39th AIAA Fluid Dynamics Conference
22 - 25 June 2009, San Antonio, Texas

AIAA 2009-3679

Numerical simulation and theoretical analysis on boundary-layer instability affected by porous coating

Xiaowen Wang * **and Xiaolin Zhong** †
Mechanical and Aerospace Engineering Department
University of California, Los Angeles, California 90095

Abstract

The effect of porous coating on the instability of a Mach 5.92 flat-plate boundary layer is investigated by a combination of numerical simulation and theoretical analysis. It is motivated by Fedorov et al.'s experimental and theoretical studies considering the effect of an ultrasonically absorptive coating on hypersonic boundary-layer stability [1] and our previous numerical simulations on hypersonic boundary-layer receptivity [2, 3]. The steady base flow is obtained by solving compressible Navier-Stokes equations with a combination of a fifth-order shock-fitting method and a second-order total variation diminishing (TVD) scheme. Stability simulations consist of two steps: 1. periodic disturbances corresponding to single boundary layer wave (mode F or mode S) are superimposed on steady base flow at a cross-section of the boundary layer to show spatial development of the wave; 2. porous coating, modelled by pressure oscillation related wall blowing-suction, is used downstream of the superimposed wave to investigate its effect on boundary-layer instability. Stability characteristics of the hypersonic boundary layer are analyzed by linear stability theory. The numerical results show that porous coating only has local effects on the spatial developments of mode S and mode F. In case of mode S, porous coating destabilizes the Mack first mode whereas it stabilizes the Mack second mode. All the six cases of stability simulations show a larger peak amplitude of mode S, which means destabilization of the Mack first mode is quite significant. In case of mode F, all three cases of stability simulations show that mode F changes to mode S near the synchronization point and mode F is generally stabilized in porous region

1 Introduction

The performance and thermal protection system of hypersonic transportation vehicles and re-entry vehicles are significantly affected by the transition of boundary-layer flows over vehicle surfaces, because a turbulent boundary layer generates much higher shear stress and heat flux to the wall than a laminar boundary layer. Controlling boundary-layer transition to maintain laminar boundary-layer flows can result in lower drag and heat flux, and higher fuel efficiency.

In order to predict and control boundary-layer transition, extensive studies have been carried out to reveal transition mechanisms [4, 5]. It is recognized that the transition of a boundary-layer flow strongly depends on the amplitude of environmental disturbance, which is schematically shown in Fig. 1. For small amplitude disturbance, the transition over a smooth surface generally consists of the following three stages: 1. receptivity process during which small amplitude environmental disturbances enter the boundary layer and excite boundary-layer waves; 2. linear development or growth of unstable boundary-layer waves which can be predicted by solving the eigen-problem of the homogeneous linearized stability equations; 3. boundary-layer transition caused by non-linear breakdown and three-dimensional effects when the unstable waves reach certain amplitudes. For high amplitude disturbance, laminar boundary-layer flow can breakdown to turbulence right after the receptivity process due to the strong initial excitations of boundary-layer waves. On non-smooth surface with roughness elements, the strong transient growth of boundary-layer wave modes may directly lead to transition. All these transitions relating to high amplitude disturbance and transient growth are called bypass transition.

*Postdoctoral Researcher,Mechanical and Aerospace Engineering Department, AIAA Member.
†Professor, Mechanical and Aerospace Engineering Department, AIAA Associate Fellow.

In hypersonic boundary layers, mode S and mode F are generally excited in receptivity process. These two waves are given the names because they are tuned to slow and fast acoustic waves, respectively, in the limit of small Reynolds numbers. Mode F and mode S were first computed by Mack [6] for the compressible Blasius boundary layer. Mack found mode F to be stable, while mode S was found to be unstable and therefore more relevant in boundary-layer transition. Mode S constitutes both the first and second modes of Mack. The first mode is an inviscid instability wave, the counterpart of the Tollmien-Schlichting (T-S) waves at low-speed flows. Because compressible boundary-layer profiles contain an inflection point, the first mode begins to dominate with the Mach number increasing. The second mode belongs to a family of trapped acoustic modes, generally occurring for Mach numbers larger than 4. Once it is excited, the second mode is more unstable than the first mode. According to the transition procedure, stabilizations of the first and second modes are critical to transition control.

Techniques used to control boundary-layer transition can be divided into two types: passive control and active control. Passive control requires modification to the mean flow to inhibit the growth of boundary-layer waves, such as controlling mean surface temperature, modifying pressure gradient, and introducing localized steady surface suction. More passive control approaches were reviewed by Saric [7]. Active control aims to suppress the environmental disturbances. For example, the wave-like disturbances can be cancelled by introducing another wave of the same amplitude but opposite phase. Thomas [8] experimentally illustrated the concept of controlling boundary-layer transition by superimposing in the flow Tollmien-Schlichting waves that were of equal amplitude and antiphased to the disturbances. In all experiments, two electromagnetically excited vibrating ribbons were used to generate the instability waves in the flow, with the first ribbon working as an excitation source and the second one as an actuator. Both hot-wire surveys and flow visualization showed that it was possible to delay transition by appropriate adjustment of the phase and amplitude of the signal driving the second ribbon. Sturzebecher and Nitsche [9] showed that a sensor-actuator system combined with an adaptive control algorithm could successfully be used to achieve a powerful attenuation of naturally excited Tollmien-Schlichting (T-S) instabilities. With a pure two dimensional control system, a local T-S wave was reduced in amplitude by about 90% . They also claimed that three-dimensional instabilities were successfully cancelled by means of a spanwise arrangement of sensors and actuators. Recently, Li and Gaster [10] numerically and experimentally investigated the control of spatially evolving three-dimensional instability waves in a flat-plate boundary layer with zero pressure gradient. They created the instability waves by computer-generated perturbations in a quiet wind tunnel, then detected the oncoming disturbances and sent appropriate control signal to the downstream actuators to generate counteracting disturbances. They achieved good agreement between experimental measurements and numerical predictions based on linear stability theory. Their results indicated that the growth of the three-dimensional instability waves could be inhibited by a simple control strategy.

Fedorov et al. [1] studied the effect of an ultrasonically absorptive coating (UAC) on hypersonic boundary-layer stability by experiment and theoretical analysis. Experiments were performed on a 7-degree half-angle sharp cone in a Mach 6 wind tunnel. Half-surface of the cone was solid whereas the other half-surface was covered by a porous coating. Both theoretical analysis and experimental results on two- and three-dimensional disturbances showed that the porous coating strongly stabilized the second mode and marginally destabilized the first mode. Since the first mode is spatially developed into the second mode downstream, destabilization of the first mode decreases the efficiency of the second mode stabilization. A straightforward solution to avoid the first mode destabilization is to move the UAC coating further downstream to a location where the second mode is dominated. In previous numerical simulations on the receptivity of a Mach 8.0 flow over a wedge to wall blowing-suction, Wang and Zhong [2] showed that the synchronization point of mode F and mode S played an important role in the excitation of mode S. Mode S was strongly excited when the blowing-suction actuator was located upstream of the synchronization point. On the other hand, when the blowing-suction actuator was downstream of the synchronization point, there was a very weak excitation of mode S, despite the fact that the blowing-suction actuator was still within the unstable region of mode S. Such results indicate that the synchronization point might be the location to start UAC coating. The accuracy of our simulations has been validated by a theoretical study carried out by Tumim, Wang, and Zhong [11]. The perturbation flow field downstream of the blowing-suction actuator was decomposed into boundary-layer waves with the help of a biorthogonal eigenfunction system. It was found that there was a good agreement between wave amplitudes calculated with the help of the theoretical receptivity model and those obtained by projecting the numerical results onto the normal waves.

In current paper, the effect of porous coating on the instability of a Mach 5.92 flat-plate boundary layer is investigated by a combination of numerical simulation and theoretical analysis. The steady base flow is obtained by solving compressible Navier-Stokes equations with a combination of a fifth-order shock-fitting method and a

second-order TVD scheme. Stability simulations consist of two steps: 1. periodic disturbances corresponding to single boundary layer wave (mode F or mode S) are superimposed on steady base flow at a cross-section of the boundary layer to show spatial development of the wave; 2. porous coating, modelled by pressure oscillation related wall blowing-suction, is used downstream of the superimposed wave to investigate its effect on boundary-layer instability. Specifically, four types of stability simulations are considered: type 1, without porous coating; type 2, porous coating located upstream of the synchronization point; type 3, porous coating located downstream of the synchronization point; type 4, porous coating located around the synchronization point. Stability characteristics of the hypersonic boundary layer are analyzed by linear stability theory.

2 Governing Equations and Numerical Methods

In the current numerical studies, a Mach 5.92 boundary layer over a flat plate as shown in Fig. 2 is considered. The flow is assumed to be thermally and calorically perfect. The governing equations for the simulation are the compressible Navier-Stokes equations in the conservative form, i.e.,

$$\frac{\partial \vec{U}^*}{\partial t^*} + \frac{\partial}{\partial x_1^*}(\vec{F}_{1i}^* + \vec{F}_{1v}^*) + \frac{\partial}{\partial x_2^*}(\vec{F}_{2i}^* + \vec{F}_{2v}^*) = 0 \tag{1}$$

where $\vec{U}^*$ is a column vector containing the conservative variables of mass, momentum, and energy, i.e.,

$$\vec{U}^* = \{\rho^*, \rho^* u_1^*, \rho^* u_2^*, e^*\}^{\mathrm{T}} \tag{2}$$

The superscript "$*$" represents dimensional variables. The flux vectors in Eq. (1) are divided into their inviscid and viscous components, because the two components are discretized with different schemes. The components, $\vec{F}_{1i}^*$ and $\vec{F}_{2i}^*$, are inviscid flux whereas $\vec{F}_{1v}^*$ and $\vec{F}_{2v}^*$ are viscous flux components. The flux components can be expressed as

$$\vec{F}_{ji}^* = \begin{bmatrix} \rho^* u_j^* \\ \rho^* u_1^* u_j^* + p^* \delta_{1j} \\ \rho^* u_2^* u_j^* + p^* \delta_{2j} \\ u_j^*(e^* + p^*) \end{bmatrix}, \quad \vec{F}_{jv}^* = \begin{bmatrix} 0 \\ -\tau_{1j}^* \\ -\tau_{2j}^* \\ -\tau_{1j}^* u_1^* - \tau_{2j}^* u_2^* - k^* \frac{\partial T^*}{\partial x_j^*} \end{bmatrix} \tag{3}$$

with $j \in \{1, 2\}$. In Eq. (3), δ_{ij} $(i = 1, 2)$ is the Kronecker Delta function. In the perfect gas assumption, pressure and energy are given by

$$p^* = \rho^* R^* T^* \tag{4}$$

$$e^* = \rho^* c_v^* T^* + \frac{\rho^*}{2}(u_1^{*2} + u_2^{*2}) \tag{5}$$

where c_v^* is the specific heat at constant volume. For compressible Newtonian flow, the viscous stress tensor can be written as:

$$\tau_{ij}^* = \mu^* \left(\frac{\partial u_i^*}{\partial x_j^*} + \frac{\partial u_j^*}{\partial x_i^*} \right) - \frac{2}{3}\mu^* \left(\frac{\partial u_1^*}{\partial x_1^*} + \frac{\partial u_2^*}{\partial x_2^*} \right) \delta_{ij} \tag{6}$$

with $i, j \in \{1, 2\}$. In the simulation, the viscosity coefficient, μ^*, and the heat conductivity coefficient, k^*, are calculated using the Sutherland's law together with a constant Prandtl number, Pr. They are both functions of temperature only.

$$\mu^* = \mu_r^* \left(\frac{T^*}{T_r^*} \right)^{3/2} \frac{T_r^* + T_s^*}{T^* + T_s^*} \tag{7}$$

$$k^* = \frac{\mu^* c_p^*}{Pr} \tag{8}$$

where $\mu_r^* = 1.7894 \times 10^{-5}$ Ns/m^2, $T_r^* = 288.0$ K, $T_s^* = 110.33$ K, and c_p^* is the specific heat at constant pressure.

The dimensional flow variables are non-dimensionalized by freestream parameters. Specifically, density, temperature, velocity, and pressure are non-dimensionalized by ρ^*_∞, T^*_∞, u^*_∞, and $\rho^*_\infty u^{*2}_\infty$. Furthermore, x^*_1 is non-dimensionalized by unit length in meter, whereas x^*_2 is non-dimensionalized by the local boundary-layer thickness, $\sqrt{\mu^*_\infty x^*_1/\rho^*_\infty u^*_\infty}$. Referring to the coordinate system shown in Fig. 2, x^*_1 and x^*_2 are x^* and y^*, respectively. The two variables, u^*_1 and u^*_2, are velocities in streamwise and wall-normal directions.

The fifth-order shock-fitting finite difference method of Zhong [12] is used to solve the governing equations in a domain bounded by the bow shock and the flat plate. In orther words, the bow shock is treated as a boundary of the computational domain. The Rankine-Hugoniot relation across the shock and a characteristic compatibility relation coming from downstream flow field are combined to solve the flow variables behind the shock. The shock-fitting method makes it possible for the Navier-Stokes equations to be spatially discretized by high-order finite difference methods. Specifically, a fifth-order upwind scheme is applied to discretize the inviscid flux derivatives. Meanwhile, a sixth-order central scheme is used for the discretization of viscous flux derivatives. By using the shock-fitting method, the interaction between the bow shock and wall forcing induced perturbations is solved as a part of solutions with the position and velocity of the shock front being taken as dependent flow variables. Temporal integration of the governing equations is calculated using Runge-Kutta method. In the leading edge region, there exists a singular point at the tip of the flat plate, which introduces numerical instability if the fifth-order shock-fitting method is used to simulate the flow. Therefore, the computational domain for the shock-fitting simulation starts from a very short distance downstream of the leading edge. A second-order TVD scheme used by Zhong and Lee [13] is applied to simulate the steady base flow in a small region including the leading edge to supply inlet conditions for the shock-fitting simulation. Stability simulations are carried out in a downstream region where the shock-fitting method can be used.

The same numerical method has been extensively used in receptivity studies of supersonic and hypersonic boundary layers over a flat plate and a sharp wedge to various freestream disturbances and surface roughness [14, 15]. The good agreement between numerical and LST results indicates that the fifth-order shock-fitting finite difference method is accurate to simulate the receptivity problems of high-speed boundary-layer flows. The numerical method has also been validated in the theoretical study and comparison with numerical simulation of Tumin, Wang, and Zhong [11].

3 Flow Conditions and Models of Porous Coating

Freestream flow conditions of the currently studied flow are the same as those of Maslov et al.'s experiment [16], i.e.,

$$M_\infty = 5.92\,, \qquad T^*_\infty = 48.69\text{K}\,,$$
$$p^*_\infty = 742.76\text{Pa}\,, \qquad Pr = 0.72\,,$$
$$f^* = 100\text{kHz}\,, \qquad \text{F} = 26.51\times 10^{-6}\,,$$
$$Re^*_\infty = 13\times 10^6/\text{m}$$

where Re^*_∞ is the unit Reynolds number defined as

$$Re^*_\infty = \rho^*_\infty u^*_\infty/\mu^*_\infty \tag{9}$$

The dimensional streamwise coordinate, x^* as shown in Fig. 2, can be converted to local Reynolds number by

$$Re_x = Re^*_\infty\ x^* \tag{10}$$

In LST studies of boundary-layer flows, the Reynolds number based on the local length scale of boundary-layer thickness, L^*, is generally used. They are expressed as

$$R = \frac{\rho^*_\infty u^*_\infty L^*}{\mu^*_\infty}, \quad L^* = \sqrt{\frac{\mu^*_\infty x^*}{\rho^*_\infty u^*_\infty}} \tag{11}$$

Hence, the relation between R and local Reynolds number Re_x is given by

$$R = \sqrt{Re_x} \tag{12}$$

For the simulation of mean flow, the wall is adiabatic, and the physical boundary condition of velocity on the flat plate is the no-slip condition. When single boundary layer wave is superimposed or porous coating is used,

the isothermal temperature condition is applied. This temperature condition is a standard boundary condition for theoretical and numerical studies of high frequency disturbances. Meanwhile, no-slip condition is applied on the wall except the porous region. Inlet conditions are specified, while high-order extrapolation is used for outlet conditions because the flow is hypersonic at the exit boundary except a small region near the flat plate. The flow variables behind the shock are solved by combining Rankine-Hugoniot relation across the shock and a characteristic compatibility relation coming from downstream flow field.

In current study, stability simulations consist of two steps: 1. periodic disturbances corresponding to single boundary layer wave are superimposed on steady base flow at a cross-section of the boundary layer to show spatial development of the wave; 2. porous coating, modelled by pressure oscillation related wall blowing-suction, is used downstream of the superimposed wave to investigate its effect on boundary-layer instability. Specifically, four types of stability simulations are considered: case 1, without porous coating; case 2, porous coating located upstream of the synchronization point; case 3, porous coating located downstream of the synchronization point; case 4, porous coating located around the synchronization point.

At step 1, disturbances corresponding to a specific boundary-layer wave at a frequency of 100 kHz are introduced at a cross-section of the boundary layer. The disturbances are a combination of velocity, pressure, and temperature oscillations, which can be expressed as,

$$\begin{Bmatrix} \tilde{u^*} \\ \tilde{v^*} \\ \tilde{w^*} \\ \tilde{p^*} \\ \tilde{T^*} \end{Bmatrix} = \epsilon \begin{Bmatrix} \hat{u^*}(y^*) \\ \hat{v^*}(y^*) \\ \hat{w^*}(y^*) \\ \hat{p^*}(y^*) \\ \hat{T^*}(y^*) \end{Bmatrix} \sin(\omega^* t^*) \tag{13}$$

where ϵ is a small dimensionless parameter representing the amplitude of disturbances. The vector, $\{\hat{u^*}(y^*)$, $\hat{v^*}(y^*)$, $\hat{w^*}(y^*)$, $\hat{p^*}(y^*)$, $\hat{T^*}(y^*)\ \}^{\mathrm{T}}$, represents the eigenfunction of the specific boundary-layer wave, which is normalized by the pressure perturbation on the wall. In above equation, ω^* is the circular frequency of the disturbances, which is related to the frequency by

$$\omega^* = 2\pi f^* \tag{14}$$

The circular frequency, ω^*, and the frequency, f^*, are non-dimensionalized according to

$$\omega = \frac{\omega^* L^*}{u^*_\infty} \tag{15}$$

$$F = \frac{2\pi f^* \mu^*_\infty}{\rho^*_\infty u^{*2}_\infty} = \frac{\omega^* \mu^*_\infty}{\rho^*_\infty u^{*2}_\infty} \tag{16}$$

With the definitions of Reynolds number R and the dimensionless frequency F, the dimensionless circular frequency can also be expressed as

$$\omega = RF \tag{17}$$

The model of the coating is the same as that of Fedorov et al. [1], i.e., blowing-suction relating to the local pressure oscillation.

$$v\prime = A_y p\prime \tag{18}$$

The porous coating admittance, A_y, is defined as

$$A_y = -\frac{\phi}{Z_0} \tanh(\Lambda h) \tag{19}$$

In above equation, ϕ is porosity, h is the porous-layer thickness non-dimensionalized by the local length scale of boundary layer thickness.

$$h = \frac{h^*}{L^*} = \frac{h^*}{\sqrt{\frac{\mu^*_\infty x^*}{\rho^*_\infty u^*_\infty}}} \tag{20}$$

Based on Allard and Champoux's theoretical analysis [17], the empirical equations for porous coating characteristic impedance (Z_0) and propagation constant (Λ) are

$$Z_0 = \frac{\rho_w}{M_e}\sqrt{\frac{T_w\tilde{\rho}}{\tilde{C}}} \tag{21}$$

$$\Lambda = \frac{i\omega M_e}{\sqrt{T_w}}\sqrt{\tilde{\rho}\tilde{C}} \tag{22}$$

where ρ_w and T_w are the local dimensionless density and temperature on coating. The edge Mach number (M_e) is defined right after the shock wave. The dynamic density ($\tilde{\rho}$) and bulk modulus ($\tilde{C}$) are calculated using the following two equations.

$$\tilde{\rho} = a_\infty[1 + \frac{g(\lambda_1)}{\lambda_1}] \tag{23}$$

$$\tilde{C} = \gamma - \frac{\gamma - 1}{1 + \frac{g(\lambda_2)}{\lambda_2}} \tag{24}$$

where λ_1, λ_2, and the function $g(\lambda)$ are defined as

$$g(\lambda) = \sqrt{1 + \frac{4a_\infty\mu_w^*\lambda}{\sigma^*\phi r_p^{*2}}} \tag{25}$$

$$\lambda_1 = \frac{ia_\infty\rho_w^*\omega^*}{\phi\sigma^*} \tag{26}$$

$$\lambda_2 = 4\mathrm{Pr}\lambda_1 \tag{27}$$

where a_∞ is the tortuosity, σ^* is the flow resistivity, and r_p^* is the characteristic pore size. These parameters are determined by the porous coating. In porous coating model, the local dimensionless variables (v, p, T_w, ρ_w, ω) are non-dimensionalized by the corresponding variables right after the shock wave (u_e^*, $\rho_e^* u_e^{*2}$, T_e^*, ρ_e^*, $\sqrt{\mu_e^* x^*/\rho_e^* u_e^*}/u_e^*$).

According to the definitions of characteristic impedance and propagation constant, the porous coating admittance is generally a complex number. And the pressure perturbation is also a complex number. However, only the real part of velocity perturbation can be imposed on the coating in numerical simulations. In this way, the velocity perturbation is written relating to the real part of pressure perturbation ($p(t^*)$) as

$$v(t^*) = \mathrm{Real}(A_y)p(t^*) - \mathrm{Imag}(A_y)p(t^* - \frac{\pi}{2\omega^*}) \tag{28}$$

where "Real(A_y)" and "Imag(A_y)" represent the real part and imaginary part of porous coating admittance, respectively.

4 Results and Discussions

4.1 Steady base flow

The steady base flow over the flat plate is simulated by solving the two-dimensional compressible Navier-Stokes equations with a combination of a fifth-order shock-fitting finite difference method and a second-order TVD scheme. In the leading edge region, there exists a singular point at the tip of the flat plate, which will introduce numerical instability if the fifth-order shock-fitting method is used to simulate the flow. Therefore, a second-order TVD scheme used by Zhong and Lee [13] is applied to simulate the steady base flow in a small region including the leading edge. The computational domain for the fifth-order shock-fitting method starts at $x^* = 0.0025$ m and ends at $x^* = 0.879$ m, corresponding to $R = 180.28$ and $R = 3380.38$, respectively. In actual shock-fitting simulations,

the computational domain is divided into 19 zones with a total of 3746 grid points in streamwise direction. The number of grid points in wall-normal direction is 121 upstream of the position of $x^* = 0.309$ m and 176 downstream of that position. Forty-one points are used in the overlapped region between two neighboring zones, which is proved to be sufficient to make the solution accurate and smooth within the whole domain. An exponential stretching function is used in the wall-normal direction to cluster more points inside the boundary layer. On the other hand, the grid points are uniformly distributed in streamwise direction. The spatial convergence of the results based on this grid structure has been evaluated by grid refinement studies to ensure the grid independence of the fifth-order shock-fitting simulations. For shock-fitting simulation in the first zone, the inlet conditions are obtained from the results of the second-order TVD shock-capturing scheme which is used to simulate the steady base flow in a small region including the leading edge. For shock-fitting simulations in other zones, inlet conditions are interpolated from the results of the previous zone.

The computational domain for the second-order TVD scheme starts at $x^* = -0.0005$ m and ends at $x^* = 0.0035$ m. Three sets of grid structures are used to check the grid independence of the numerical results. Figure 3 compares the density distributions in wall-normal direction. In this figure, the density distributions are evaluated at $x^* = 0.0025$ m, the initial location of the first zone. It shows that density distribution on 201×176 mesh agrees well with that on 241×181 mesh whereas it has significant discrepancies with that on 161×101 mesh. This figure indicates that the grid structure of 201×176 is fine enough to ensure the grid independence of numerical results. However, the grid structure of 161×101 is too coarse to achieve spatially converged numerical results.

In order to validate the combination of fifth-order shock-fitting method and second-order TVD scheme, Fig. 4 plots density contours near the leading edge of the steady base flow obtained by the combination of second-order TVD scheme and fifth-order shock-fitting method. The flow field including the leading edge is simulated by the TVD scheme, while the flow field after $x^* = 0.0025$ m is simulated by the shock-fitting method. These figures show that density contours calculated by the two methods have a good agreement near the upstream edge of the overlapped region, which indicates that the TVD solutions are accurate enough to be used as inlet conditions for the fifth-order shock-fitting simulation in the first zone. The small discrepancies of the contours near the bow shock are caused by viscous effect. Due to viscosity, the bow shock has a finite thickness for TVD simulation, while it is assumed to be infinitely thin for the shock-fitting simulation.

Figures 5(a) and 5(b) shows pressure contours of steady base flow computed by the fifth-order shock-fitting method. In Fig. 5(a), the upper boundary of flow field represents bow shock induced by displacement thickness of the boundary layer. The lower boundary is the flat plate. A part of pressure contours from $x^* = 0.33$ m to $x^* = 0.36$ m ($R = 2071.23$ to $R = 2163.33$) is amplified in Fig. 5(b) to show clearly pressure distributions within the boundary layer. It is noticed that pressure is approximately a constant across the boundary layer and along the Mach lines, which is consistent with boundary layer theory and inviscid supersonic aerodynamics. At a fixed location (constant x^*), pressure behind the shock is higher than that on flat plate due to the existence of bow shock. Figure 6 shows distributions of wall pressure and pressure behind bow shock computed by the fifth-order shock-fitting method. Large pressure gradient near the leading edge is caused by the interaction between viscous boundary layer and inviscid outer flow. From upstream to downstream, viscous-inviscid interaction becomes weaker with bow shock moving away from the boundary layer. As a result, pressure approaches a constant further downstream with pressure gradient decreasing. Again, Fig. 6 shows that at a fixed location (constant x^*), pressure behind the shock is higher than that on flat plate.

Figure 7 shows bow shock position and distribution of Mach number behind the shock. In this figure, a straight line tangential to shock near the leading edge is plotted helping to illustrate that the shock is not a straight line. Decrease of shock angle from upstream to downstream indicates that the shock becomes weaker downstream. The dramatic increase of Mach number near the leading edge is also due to interaction between viscous boundary layer and inviscid outer flow. After $x^* = 33$ mm ($R = 654.98$), intensity of viscous-inviscid interaction decreases quickly with blow shock moving away from the boundary layer. Mach number behind the shock approaches a constant downstream. The increase of Mach number also indicates that bow shock becomes weaker from upstream to downstream.

The accuracy of the steady base flow has been validated by comparisons with Maslov et al.'s experimental measurements [16] and the self-similar boundary-layer solution. Details of the validation is neglected here whereas they can be found in Wang and Zhong's recent paper [18].

4.2 Stability characteristics of boundary-layer wave modes

The stability characteristics of boundary-layer waves of the Mach 5.92 flow is studied by LST based on a multi-domain spectral method of Malik [19]. The velocity, pressure, and temperature disturbances are represented by harmonic waves of the form

$$\begin{Bmatrix} \tilde{u} \\ \tilde{v} \\ \tilde{w} \\ \tilde{p} \\ \tilde{T} \end{Bmatrix} = \begin{Bmatrix} \hat{u}(y) \\ \hat{v}(y) \\ \hat{w}(y) \\ \hat{p}(y) \\ \hat{T}(y) \end{Bmatrix} e^{i(\alpha_c x + \beta_c z - \omega_c t)} \tag{29}$$

The parameters of α_c and β_c are wave number components in streamwise and spanwise directions, and ω_c is the circular frequency. For two-dimensional wall perturbations, $\beta_c = 0$. Substituting disturbances of Eq. (29) and the steady base flow into the compressible linearized Navier-Stokes equations, an ordinary-differential-equation system is achieved, i.e.,

$$(A\frac{d^2}{dy^2} + B\frac{d}{dy} + C)\phi = 0 \tag{30}$$

where ϕ is the disturbance vector defined by $\{\hat{u}, \hat{v}, \hat{p}, \hat{T}, \hat{w}\}^{\mathrm{T}}$. The coefficient matrices of A, B, and C are given in Malik's paper [19]. In spatial stability analysis, the two parameters, ω_c and β_c, are specified as real numbers. The streamwise wave number, α_c, is a complex number and solved as the eigenvalue of the ordinary-differential-equation system. The complex wave number α_c can be expressed as

$$\alpha_c = \alpha_r - i\alpha_i \tag{31}$$

where α_i is the local growth rate. A boundary-layer wave is unstable when $\alpha_i < 0$ whereas it is stable when $\alpha_i > 0$. The points $\alpha_i = 0$ are called the neutral points of the boundary-layer wave. A wave is generally unstable only in certain domains bounded by the neutral points. The real part, α_r, is the local wave number which can be used to define the local phase velocity:

$$a = \frac{\omega_c}{\alpha_r} \tag{32}$$

Both the wave number and the phase velocity can be used to identify the boundary-layer wave.

Figure 8 shows eigenvalue spectra of wave number α of the boundary-layer waves for a case with a frequency of $f^* = 100$ kHz at $x^* = 0.189$ m ($F = 53.03 \times 10^{-6}$, $R = 1567.48$). The figure shows the wave spectra corresponding to fast acoustic waves, entropy and vorticity waves, and slow acoustic waves. The two discrete modes marked by circles are mode F and mode S. Mode F is a stable mode, which originates from the fast acoustic spectrum on the left side of the figure and passes the entropy and vorticity spectra at the center as dimensionless frequency increases. Mode S originates from the slow acoustic spectrum on the right side of the figure. It becomes unstable in certain range of dimensionless frequency. The figure also shows that mode S at the frequency of $f^* = 100$ kHz is unstable at $x^* = 0.189$ m with $\alpha_i < 0$.

Figure 9 shows the dimensionless phase velocities of boundary-layer wave modes at two locations of $x^* = 0.159$ m and $x^* = 0.189$ m as a function of the dimensionless circular frequency. The three horizontal dashed lines represent the dimensionless phase velocities of fast acoustic wave ($a = 1 + M_\infty^{-1}$), entropy and vorticity waves ($a = 1$), and slow acoustic wave ($a = 1 - M_\infty^{-1}$), respectively. The excellent agreement of the phase velocities at different locations indicates that the phase velocity is approximately a function of dimensionless circular frequency only. The figure clearly shows that mode F originates from fast acoustic mode. As ω increases, the phase velocity of mode F decreases. When mode F passes the continuous entropy and vorticity modes near $\omega = 0.1$, there exists a jump of phase velocity, which is consistent with the theoretical analysis of Fedorov and Khokhlov [20]. On the other hand, mode S originates from slow acoustic mode. The figure also shows that mode S synchronizes with mode F at the point of $\omega_s = 0.11563$ and $a_s = 0.93076$. The synchronization location in x^* coordinate for a given dimensionless frequency can be calculated using the following formula

$$x_s^* = \frac{(\omega_s/F)^2}{Re_\infty^*} \tag{33}$$

At the synchronization point, dimensionless phase velocities of mode S and mode F are the same, and their eigenfunctions have similar profiles as shown in Fig. 10. In this figure, flow fluctuations, p'_r and u'_r, in wall-normal direction are normalized by pressure fluctuation on the wall. The figure shows that flow fluctuations are confined within the boundary layer. Except the differences near edge of the boundary layer, eigenfunctions of mode F and mode S agree very well at the synchronization point.

Figure 11 shows the growth rates of mode S and mode F at the same set of locations as a function of the dimensionless circular frequency ω. The horizontal dotted line stands for the neutral modes ($\alpha_i = 0$). In Fig. 11, the growth rates of mode S of the two locations agree well, and they are approximately functions of ω only. Mode S is unstable in the region from $\omega_I = 0.00827$ to $\omega_{II} = 0.18465$. The parameters ω_I and ω_{II} are called the Branch I and Branch II neutral points of mode S. The figure shows that mode S is stable upstream of Branch I neutral point and downstream of Branch II neutral point. The locations of the Branch I and Branch II neutral points in x^* coordinate, which changes with different dimensionless frequencies, can be calculated by

$$x^*_I = \frac{(\omega_I/F)^2}{Re^*_\infty} \tag{34}$$

$$x^*_{II} = \frac{(\omega_{II}/F)^2}{Re^*_\infty} \tag{35}$$

For the boundary layer waves considered in current paper, the synchronization point and the two neutral points in x^* coordinate are respectively located at 0.33184 m, 1.69744×10^{-3} m, and 0.84622 m.

4.3 Spatial developments of mode S and mode F

As has been mentioned, stability simulations consist of two steps: 1. periodic disturbances corresponding to single boundary layer wave (mode F or mode S) are superimposed on steady base flow at a cross-section of the boundary layer to show spatial development of the wave; 2. porous coating is used downstream of the superimposed wave to investigate its effect on boundary-layer instability. In this section, spatial developments of mode S and mode F are studied.

Periodic disturbances corresponding to mode S or mode F at a frequency of 100 kHz is superimposed on steady base flow at a cross-section of the boundary layer at $x^* = 69.00$ mm. The computational domain for stability simulation starts at $x^* = 69.00$ mm and ends at $x^* = 0.8590$ m. The parameters of disturbance amplitude, ϵ in Eq. (13), are assigned to mode S and mode F as 1.0×10^{-8} and 1.0×10^{-6}, respectively. These two values are small enough to preserve the linear properties of the disturbances. Figure 12 compares superimposed disturbances of mode S with the eigenfunctions of mode S obtained from LST. Similar comparisons of mode F are shown in Fig. 13. In these figures, both superimposed disturbances and the eigenfunctions are normalized by corresponding pressure disturbance on the wall. The good agreements of velocity and pressure profiles indicate that the disturbances superimposed across the boundary layer are exactly mode S or mode F. The discrepancy between temperature profiles near the wall ($y/L < 10$) as shown in Figs. 12(d) and 13(d) is caused by nonparallel flow effect. Temperature profile of superimposed disturbance is calculated using pressure and density eigenfunctions of corresponding wave, and mean flow temperature, pressure, and density, i.e.,

$$\tilde{T^*} = T^*_0(\frac{\tilde{p^*}}{p^*_0} - \frac{\tilde{\rho^*}}{\rho^*_0}) \tag{36}$$

where T^*_0, p^*_0, and ρ^*_0 are mean flow temperature, pressure, and density. $\tilde{p^*}$ and $\tilde{\rho^*}$ are pressure and density components of the eigenfunction. Nonparallel flow effect is included in mean flow variables.

Figure 14 shows the spatial developments of superimposed mode S and mode F. In this figure, the spatial development of superimposed mode F with an amplitude parameter being 1.0×10^{-8} is also plotted. It is clearly shown that the spatial developments of mode F with different amplitudes have the same profile. One hundred times difference in superimposed disturbance amplitude leads to 100 times amplitude difference in spatial development, which illustrates the linear properties of disturbances. After mode S is superimposed at $x^* = 69.00$ mm, it grows dramatically with the peak of amplitude being around $x^* = 0.8$ m. The scenario of mode F is quite different from that of mode S. After the transient process, amplitude of mode F is decreasing because mode F is a stable wave. The lowest amplitude of mode F is observed at around $x^* = 0.24$ m. Then the wave grows quite similar to mode S, also with the peak of amplitude being around $x^* = 0.8$ m.

In order to investigate the spatial development of superimposed waves quantitatively, a local wave number (α_r) and a local growth rate (α_i) related to pressure perturbation along the flat plate are calculated,

$$\alpha_r = L^* \frac{d\phi'}{dx^*} \tag{37}$$

$$\alpha_i = -\frac{L^*}{|p'|} \frac{d|p'|}{dx^*} \tag{38}$$

where L^* is the length scale of local boundary layer thickness as defined by Eq. (11). $|p'|$ and ϕ' are pressure perturbation amplitude and phase angle, respectively. The parameters α_r and α_i will represent the true wave number and growth rate only if the perturbation is dominated by a single wave mode. Otherwise, the disturbance needs to be decomposed in odrer to check properties of a specific mode. For example, Tumin, Wang, and Zhong [11] decomposed the disturbance at a location just downstream of the blowing-suction actuator with a biorthogonal eigenfunction system, where mode F, mode S, and acoustic modes coexisted and none of them was dominant.

Since only one boundary layer wave is superimposed in stability simulations, the superimposed wave is dominant in the boundary layer. In this case, Eqs. (37) and (38) can be used to check the properties of the superimposed wave. Figure 15 compares the growth rate calculated from stability simulations with that obtained from LST for superimposed mode S and mode F. For mode S, the growth rate of stability simulation has a good agreement with that of LST in the region from $\omega = 0.11$ to $\omega = 0.13$. When ω is larger than 0.13, the growth rate of stability simulation is larger than that of LST, i.e., mode S obtained by stability simulation becomes more stable than that predicted by LST. For mode F, the figure shows that the growth rate of stability simulation initially has a good agreement with that of LST. However, it approaches that of mode S near the synchronization point, which indicates that mode F changes to mode S near the synchronization point. After the change, the growth rate of stability simulation has a good agreement with that of mode S. The discrepancy between the growth rates of mode S calculated from stability simulation and LST, when ω is larger than 0.13, is mainly caused by the nonparallel flow effect.

Figure 16 compares the phase velocity calculated from stability simulations with that obtained from LST for superimposed mode S and mode F. For mode S, the agreement of the two sets of phase velocities in downstream region of $x^* > 0.30$ m confirms that mode S is the dominant wave in the boundary layer. It is clearly shown that the phase velocity of mode F has strong oscillations around $x^* = 0.24$, where mode F is synchronized with vorticity and entropy waves. This synchronization leads to the initial growth of mode F around $x^* = 0.24$. After $x^* = 0.32$ m, the phase velocity of mode F approaches that of mode S, which indicates that mode F changes to mode S. Figure 17 compares pressure perturbation profiles across the boundary layer at two locations, $x^* = 249$ mm and $x^* = 359$ mm, for superimposed mode S and mode F. The two locations are upstream and downstream of the synchronization point ($x^* = 0.33184$ m), respectively. The figure shows significant difference between pressure perturbation profiles at $x^* = 249$ mm. Whereas pressure perturbation profiles have a good agreement at $x^* = 359$ mm. This figure confirms that mode F changes to mode S after the synchronization point.

4.4 Effect of porous coating on mode S

At the second step of stability simulations, porous coating, modelled by pressure oscillation related wall blowing-suction, is used downstream of the superimposed wave to investigate its effect on boundary-layer instability. In current study, parameters of porous coating are the same as those used in Fedorov et al.'s paper [1], i.e.,

$$\begin{aligned} &\phi = 0.75\,, && h^* = 0.75\text{mm}\,,\\ &a_\infty = 1\,, && d^* = 30\mu\text{m}\,,\\ &\sigma^* = 1.66\times 10^5 \text{kg}(\text{m}^3\text{s}^{-1})\,, && \gamma = 1.4 \end{aligned}$$

where d^* is the fiber diameter, which is related to the characteristic pore size as follows:

$$r_p^* = \frac{\pi d^*}{2 - 3\phi + \phi^2} \tag{39}$$

Four types of stability simulations are considered: type 1, without porous coating; type 2, porous coating located upstream of the synchronization point; type 3, porous coating located downstream of the synchronization point;

type 4, porous coating located around the synchronization point. The locations of porous coating for the four types are schematically shown in Fig. 18. Type 1 stability simulation, the spatial developments of mode S and mode F without porous coating, has been discussed in previous section.

Specifically, six cases of stability simulations are considered to investigate the effect of porous coating and its location on mode S. For the six cases considered, porous coating is used both upstream and downstream of the synchronization point, with its locations being as follows,

- Case 1: one porous coating at $(73.5, 124.8)$ mm;
- Case 2: two porous coatings at $(73.5, 124.8)$ mm and $(193.5, 244.8)$ mm;
- Case 3: three porous coatings, the third at $(283.5, 304.8)$ mm, the first two are the same as those in Case 2;
- Case 4: four porous coatings, the fourth at $(366.5, 402.0)$ mm, the first three are the same as those in Case 3;
- Case 5: five porous coatings, the fifth at $(466.5, 502.0)$ mm, the first four are the same as those in Case 4;
- Case 6: six porous coatings, the sixth at $(574.0, 645.0)$ mm, the first five are the same as those in Case 5;

Figures 19 shows amplitude distributions of pressure perturbation along the flat plate for the six cases of porous coating, together with the spatial development of mode S. It is noticed that pressure perturbations of all the six cases with porous coating have a similar profile as that of purely mode S without porous coating, both having the peak of amplitude at around $x^* = 0.8$ m. However, porous coating does affect the amplitude of mode S. For cases 1 to 3, porous coatings are upstream of the synchronization point. Amplitude of pressure perturbation increases with the number of porous coating increasing from case 1 to case 3. For cases 4 to 6, porous coatings except the first three are downstream of the synchronization point. Amplitude of pressure perturbation decreases with the number of porous coating increasing from case 4 to case 6. The results show that porous coating destabilizes the Mack first mode whereas it stabilizes the Mack second mode, which is consistent with Fedorov et al.'s experimental and theoretical studies [1]. In Egorov et al.'s numerical simulations on the receptivity of a Mach 6 boundary layer over a flat plate with porous coating [21], when mode S was excited by a slow acoustic wave, porous coating was found to slightly destabilize the Mack first mode and stabilize the Mack second mode. Eventually, porous coating lead to a smaller peak amplitude of mode S. Here all the six cases of stability simulations show a larger peak amplitude of mode S, which means destabilization of the Mack first mode is quite significant. In order to control boundary layer transition, it is very important to put porous coating downstream of the synchronization point, where mode S corresponds to the Mack second mode.

Figure 20 shows amplification ratios of porous coating on the spatial development of mode S. In the figure, amplification (Ap) and relative amplification (Rap) of pressure perturbation are calculated according to the following formula,

$$\mathrm{Ap} = (p_i - p_0)/p_0 * 100\% \quad (i = 1, 2, 3, 4, 5, 6) \tag{40}$$

$$\mathrm{Rap} = (p_i - p_{i-1})/p_{i-1} * 100\% \quad (i = 1, 2, 3, 4, 5, 6) \tag{41}$$

where case number "0" stands for the spatial development of mode S without porous coating. From the above definitions, it is clear that, for a specific case i, amplification ratio stands for the effect of all the i porous coatings whereas relative amplication ratio stands for the effect of ith porous coating only. The figure shows that porous coating amplifies the pressure perturbation in all the six cases. For cases 1 to 3, porous coatings are upstream of the synchronization point, and relative amplifications are positive. For cases 4 to 6, porous coatings except the first three are downstream of the synchronization point, and relative amplifications are negative. These results indicate that porous coating destabilizes the Mack first mode whereas it stabilizes the Mack second mode. It is also shown in the figure that the second porous coating is most efficient in the Mach first mode destabilization whereas the fourth porous coating is most efficient in the Mach second mode stabilization.

Figure 21 compares the growth rate calculated from stability simulations with that obtained from LST for the six cases of porous coating, together with the spatial development of mode S. The growth rate for stability simulations with porous coating are quite similar to that of purely mode S without porous coating. They all have a good agreement with that of LST in the region from $\omega = 0.11$ to $\omega = 0.13$. When ω is larger than 0.13, the

growth rate of numerical simulation results are larger than that of LST. Figure 22 compares the phase velocity calculated from stability simulations with that obtained from LST for the six cases of porous coating, together with the spatial development of mode S. The agreement of the two sets of phase velocities in downstream region of $x^* > 0.30$ m confirms that mode S is the dominant wave in the boundary layer. The agreement in phase velocity is not so good in regions where porous coating are used. These two figures show that porous coating only has a local effect on mode S.

4.5 Effect of porous coating on mode F

In this section, three cases of stability simulations are considered to investigate the effect of porous coating and its location on mode F. The locations of porous coating for the three cases are as follows,

- Case 1: one porous coating at $(73.65, 124.65)$ mm;
- Case 2: two porous coatings at $(73.65, 124.65)$ mm and $(193.65, 244.65)$ mm;
- Case 3: three porous coatings, the third at $(283.65, 304.65)$ mm, the first two are the same as those in Case 2;

For all three cases, porous coating is upstream of the synchronization. The cases with porous coating being downstream of the synchronization point is not considered, because mode F changes to mode S after the synchronization point. The effect of porous coating on mode S has been studied in previous section. Figures 23 shows amplitude distributions of pressure perturbation along the flat plate for the three cases of stability simulations, together with the spatial development of mode F. It is noticed that porous coating increases pressure perturbation amplitude downstream of the porous region. With the number of porous coatings increasing from case 1 to case 3, pressure perturbation amplitude keeps increasing.

To show clearly the spatial development of mode F in porous region, Figure 24 compares pressure perturbation amplitude obtained from stability simulation with porous coating with that of mode F without porous coating. This figure shows that the effect of porous coating on mode F in porous region depends on the location of porous coating. For porous coating located in the region $(73.65, 124.65)$ mm, pressure perturbation amplitude decreases in the whole region. Similar phenomenon is observed for porous coating located in the region $(283.65, 304.65)$ mm. However for porous coating located in the region $(193.65, 244.65)$ mm, pressure perturbation amplitude decreases initially then increases near the trailing edge of the porous region. The increase of mode F at $x^* = 0.24$ is caused by the synchronization of mode F and vorticity and entropy waves. Generally, porous coating decreases pressure perturbation in porous region, i.e., porous coating stabilizes mode F in porous region.

Figure 25 compares the growth rate calculated from stability simulations with that obtained from LST for the three cases of porous coating, together with the spatial development of mode F. The growth rate for stability simulations with porous coating are quite similar to that of purely mode F without porous coating. All cases show that mode F changes to mode S near the synchronization point. After the change, the growth rate of stability simulations has a good agreement with that of LST for mode S. Figure 26 compares the phase velocity calculated from stability simulations with that obtained from LST for the three cases of porous coating, together with the spatial development of mode S. It is clearly shown that mode F changes to mode S around $x^* = 0.32$ m. The agreement of the two sets of phase velocities in downstream region of $x^* > 0.30$ m confirms that mode S is the dominant wave in the boundary layer. These two figures also show that porous coating only has a local effect on mode F.

5 Summary

The effect of porous coating on the instability of a Mach 5.92 flat-plate boundary layer is investigated by a combination of numerical simulation and theoretical analysis. The steady base flow is obtained by solving compressible Navier-Stokes equations with a combination of a fifth-order shock-fitting method and a second-order TVD scheme. Stability simulations consist of two steps: 1. periodic disturbances corresponding to single boundary layer wave are superimposed on steady base flow at a cross-section of the boundary layer to show spatial development of the wave; 2. porous coating is used downstream of the superimposed wave to investigate its effect on boundary-layer instability. The same theoretical model of porous coating as that in Fedorov et al.'s paper is used, i.e., porous coating is modelled by pressure perturbation related wall blowing-suction. Stability characteristics of the hypersonic

boundary layer are analyzed by linear stability theory. The numerical results show that porous coating only has local effects on the spatial developments of mode S and mode F. In case of mode S, porous coating destabilizes the Mack first mode whereas it stabilizes the Mack second mode. All the six cases of stability simulations show a larger peak amplitude of mode S, which means destabilization of the Mack first mode is quite significant. In case of mode F, all three cases of stability simulations show that mode F changes to mode S near the synchronization point and mode F is generally stabilized in porous region. In order to control boundary layer transition, it is very important to put porous coating downstream of the synchronization point, where mode S corresponds to the Mack second mode.

Acknowledgments

This work was sponsored by the AFOSR/NASA National Center for Hyersonic Research in Laminar-Turbulent Transition and by the Air Force Office of Scientific Research, USAF, under Grants No. FA9550-07-1-0414 and FA9550-04-1-0029, monitored by Dr. John Schmisseur. The views and conclusions contained herein are those of the authors and should not be interpreted as necessarily representing the official policies or endorsements either expressed or implied, of the Air Force Office of Scientific Research or the U.S. Government.

References

[1] A. Fedorov, A. Shiplyuk, A. Maslov, E. Burov, and N. Malmuth. Stabilization of a hypersonic boundary layer using an ultrasonically absorptive coating. *Journal of Fluid Mechanics*, Vol. 479, pp. 99-124, 2003.

[2] X. Wang and X. Zhong. Receptivity of A Mach 8.0 Flow over A Sharp Wedge to Wall Blowing-Suction. *AIAA paper 2005-5025*, June 2005.

[3] X. Wang and X. Zhong. Role of the synchronization point on boundary layer stabilization using porous coating. *AIAA paper 2008-4382*, June 2008.

[4] M. V. Morkovin, E. Reshotko, and T. Herbert. Transition in open flow systems - a reassessment. *Bulletin of the American Physical Society*, Vol. 39, pp. 1882, 1994.

[5] E. Reshotko. Is Re_θ/Me a meaningful transition criterion ? *AIAA Journal*, 45(7), 1441, 2007.

[6] L. M. Mack. Boundary layer linear stability theory. In *AGARD report, No. 709*, pages 3–1 to 3–81, 1984.

[7] W. S. Saric. Laminar-turbulent transition: fundamentals. *AGARD R-786*, 1992.

[8] A. S. W. Thomas. The control of boundary-layer transition using a wave-superposition principle. *Journal of Fluid Mechanics*, Vol. 137, pp. 233-250, 1983.

[9] D. Sturzebecher and E. Nitsche. Active control of boundary-layer instabilities on an unswept wing. *Notes on Numerical Fluid Mechanics and Multidisciplinary Design*, Vol. 86, pp. 189-202, 2003.

[10] Y. Li and M. Gaster. Active control of boundary-layer instabilities. *Journal of Fluid Mechanics*, Vol. 550, pp. 185-205, 2006.

[11] A. Tumin, X. Wang, and X. Zhong. Direct numerical simulation and the theory of receptivity in a hypersonic boundary layer. *Physics of Fluids*, Vol. 19, Paper No. 014101, 2007.

[12] X. Zhong. High-Order Finite-Difference Schemes for Numerical Simulation of Hypersonic Boundary-Layer Transition. *Journal of Computational Physics*, Vol.144, pp. 662-709, 1998.

[13] X. Zhong and T. Lee. Nonequilibrium real-gas effects on disturbance/bow shock interaction in hypersonic flow past a cylinder. *AIAA paper 1996-1856*, January 1996.

[14] Y. Ma and X. Zhong. Receptivity of a supersonic boundary layer over a flat plate. Part 3. Effects of different types of free-stream disturbances. *Journal of Fluid Mechanics*, Vol.532, pp.63-109, 2005.

[15] X. Wang and X. Zhong. Receptivity of a hypersonic flat-plate boundary layer to three-dimensional surface roughness. *Journal of Spacecraft and Reckets*, Vol. 45, No. 6, pp. 1165-1174, 2008.

[16] A. A. Maslov, A. N. Shiplyuk, A. Sidorenko, and D. Arnal. Leading-edge receptivity of a hypersonic boundary layer on a flat plate. *Jounral of Fluid Mechanics*, Vol.426, pp.73-94, 2001.

[17] J-F. Allard and Y. Champoux. New empirical equations for sound propagation in rigid frame fibrous materials. *The Journal of the Acoustical Society of America*, Vol. 91, No. 6, pp. 3346-3353, 1992.

[18] X. Wang and X. Zhong. Effect of wall perturbations on the receptivity of a hypersonic boundary layer. *Physics of Fluids*, Vol. 21, Paper No. 044101, 2009.

[19] M. R. Malik. Numerical methods for hypersonic boundary layer stability. *Journal of Computational Physics*, Vol.86, pp.376-413, 1990.

[20] A. V. Fedorov and A. P. Khokhlov. Prehistory of Instability in a Hypersonic Boundary Layer. *Theoretical and Computational Fluid Dynamics*, Vol. 14, pp. 359-375, 2001.

[21] I. V. Egorov, A. V. Fedorov, and V. G. Soudakov. Receptivity of a hypersonic boundary layer over a flat plate with a porous coating. *Journal of Fluid Mechanics*, Vol. 601, pp. 165-187, 2008.

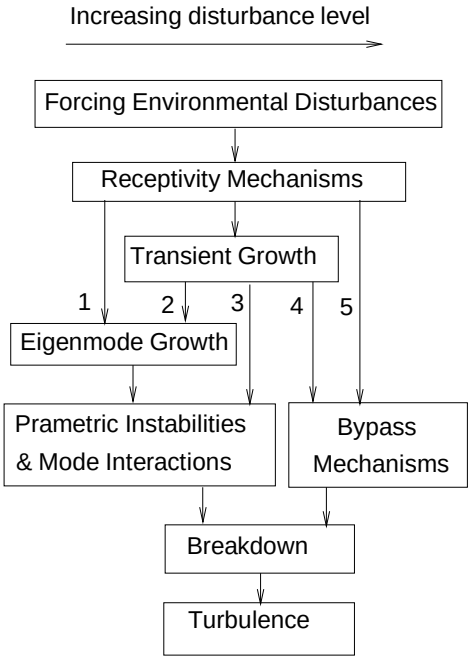

Figure 1: Paths of the boundary layer transition respecting to the amplitude of environmental disturbance.

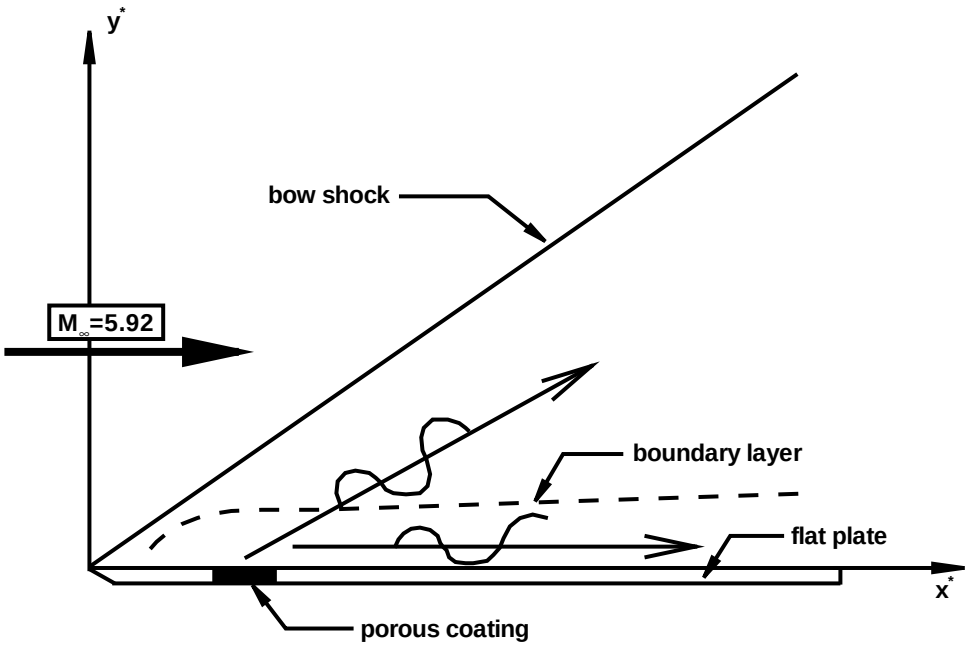

Figure 2: A schematic of the control of a Mach 5.92 flow over a flat plate with porous coating.

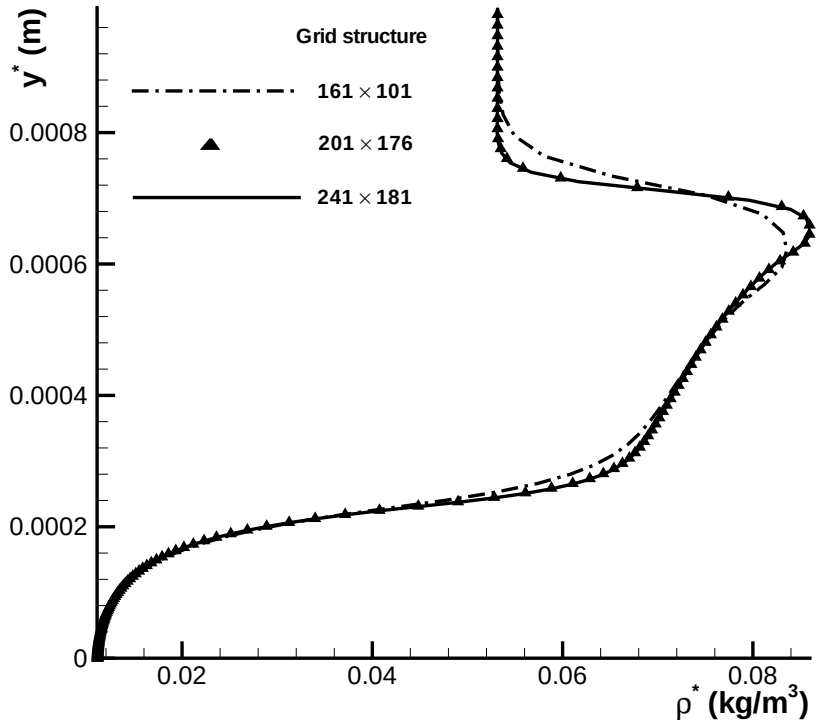

Figure 3: Comparison of density distributions in wall-normal direction at $x^* = 0.0025$ m simulated by second-order TVD scheme based on three sets of grid structures.

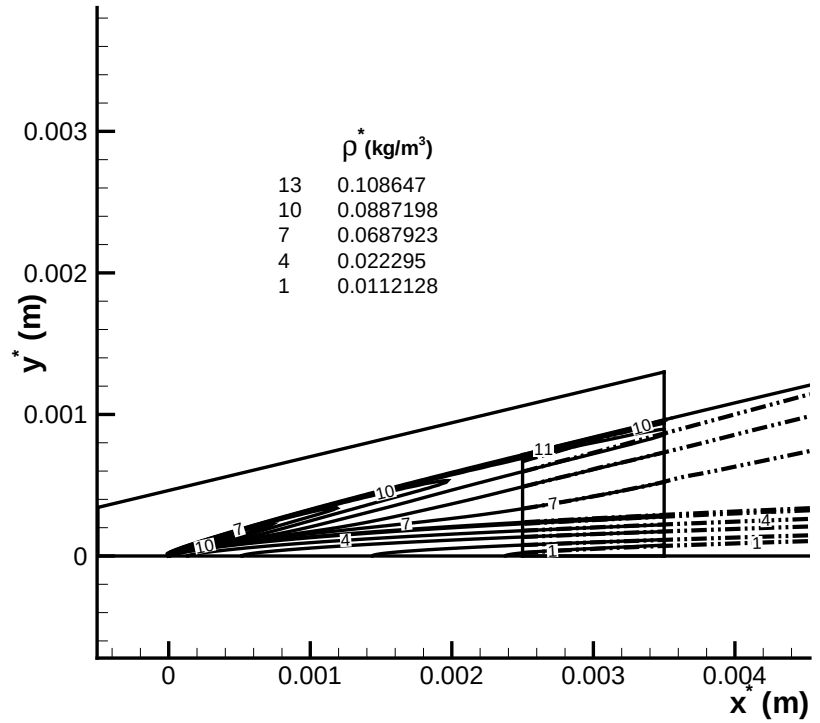

Figure 4: Density contours near the leading edge of the steady base flow obtained by the combination of second-order TVD scheme and fifth-order shock-fitting method.

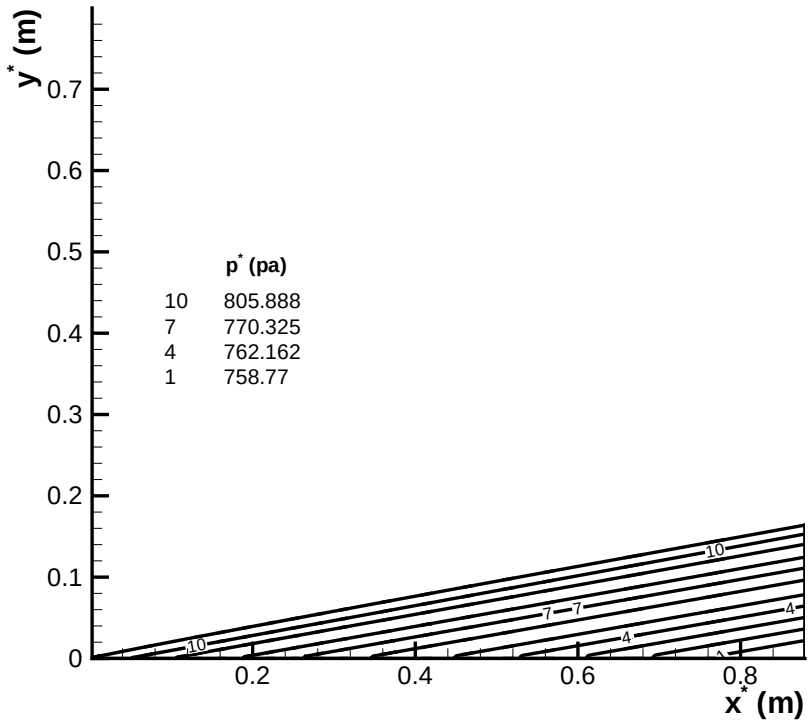

(a)

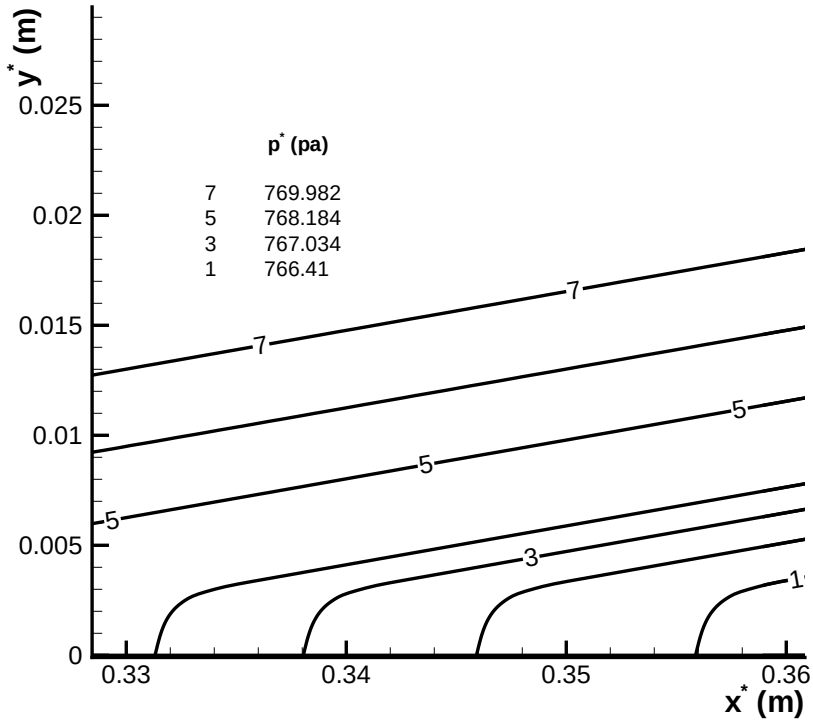

(b)

Figure 5: Pressure contours of steady base flow computed by the fifth-order shock-fitting method.

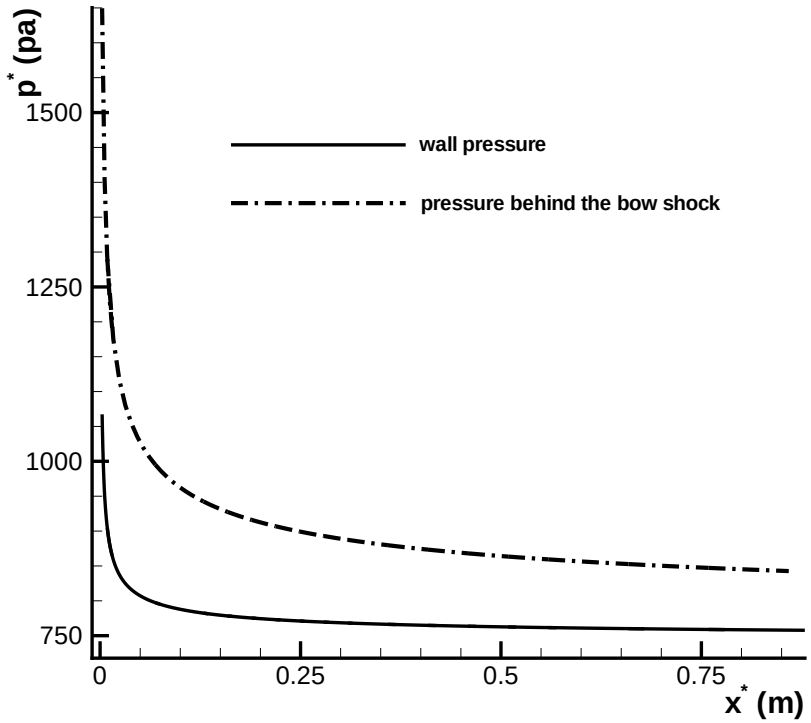

Figure 6: Distributions of wall pressure and pressure behind the shock.

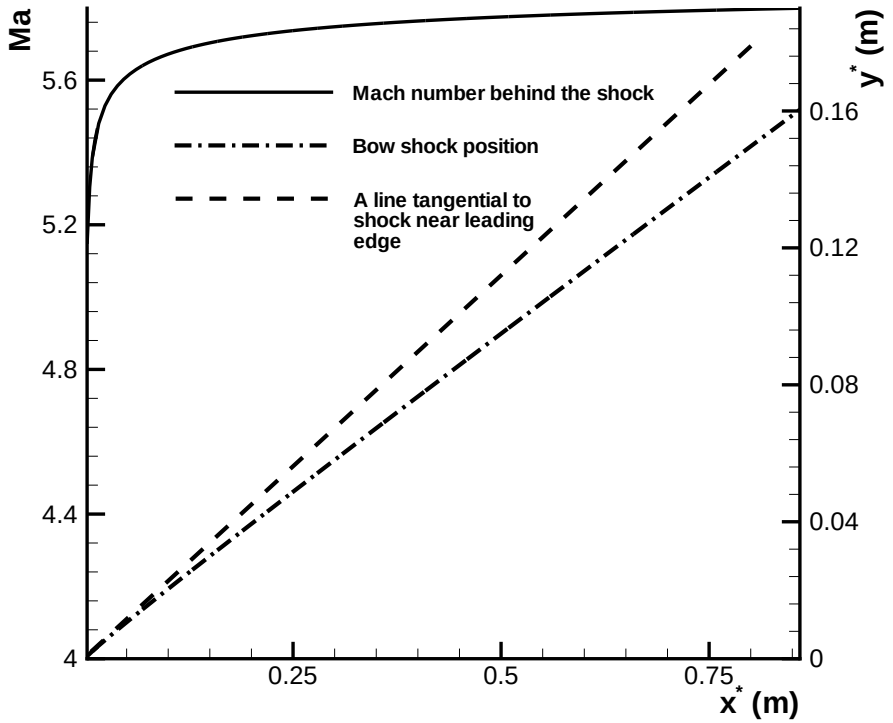

Figure 7: Shock position and distribution of Mach number behind the shock.

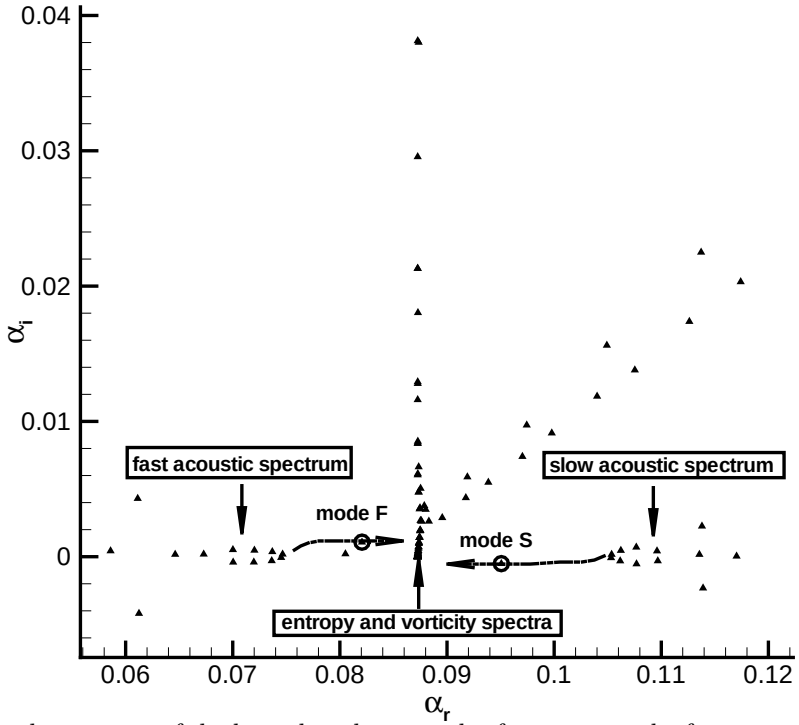

Figure 8: Eigenvalue spectra of the boundary-layer modes for a case at the frequency of $f^* = 100$ kHz at $x^* = 0.189$ m.

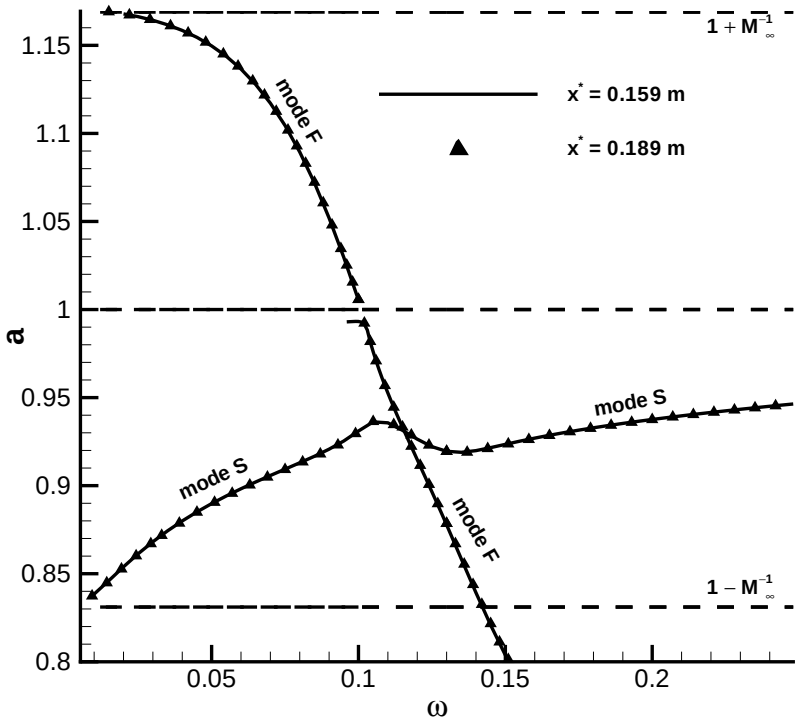

Figure 9: Distributions of dimensionless phase velocities of boundary-layer wave modes at two different locations versus dimensionless circular frequency.

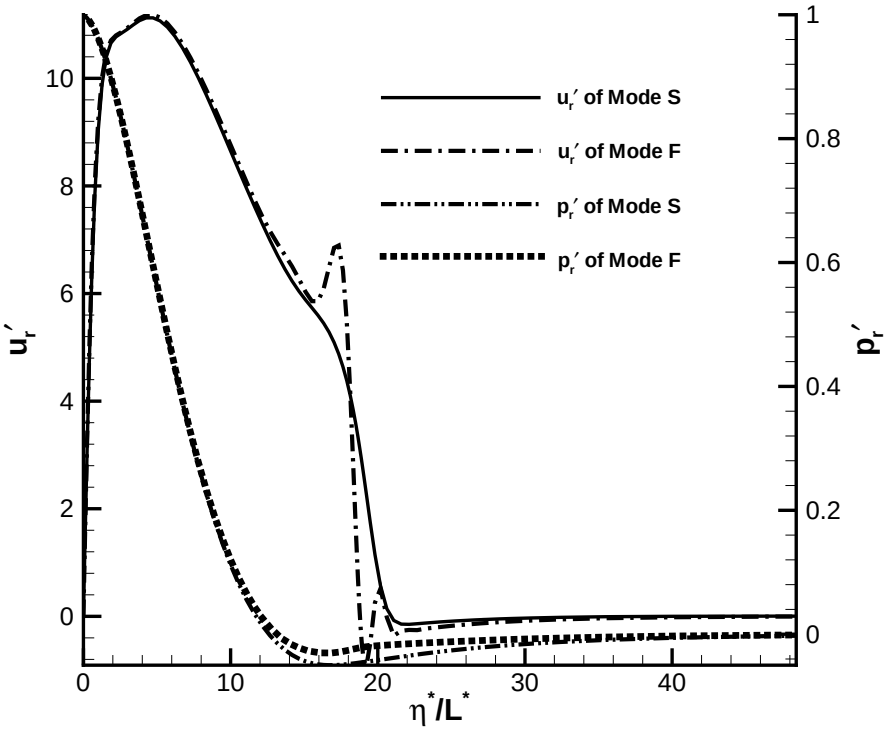

Figure 10: Eigenfunctions of streamwise velocity and pressure of mode F and mode S at the synchronization point.

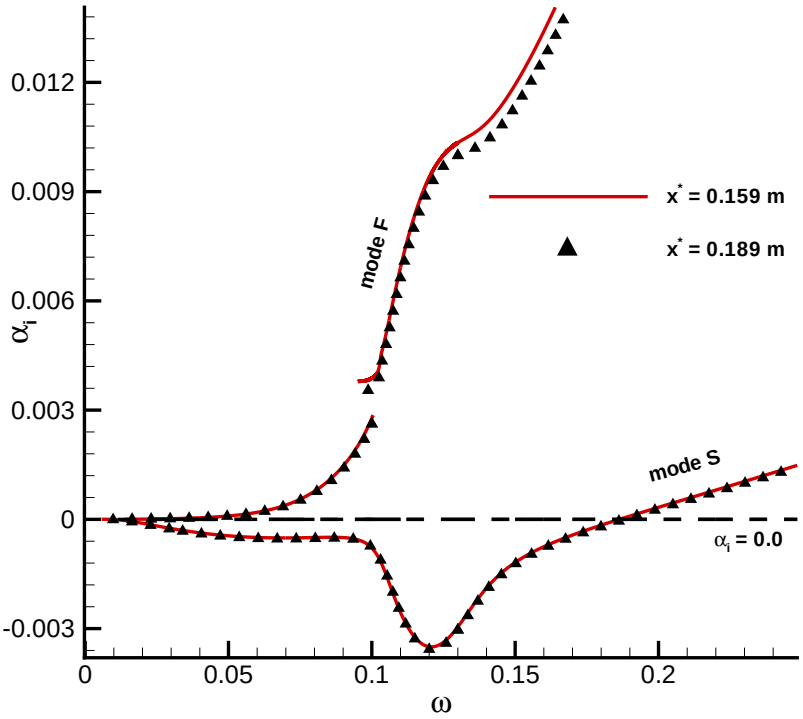

Figure 11: Distributions of growth rates of mode S and mode F at the two locations versus ω.

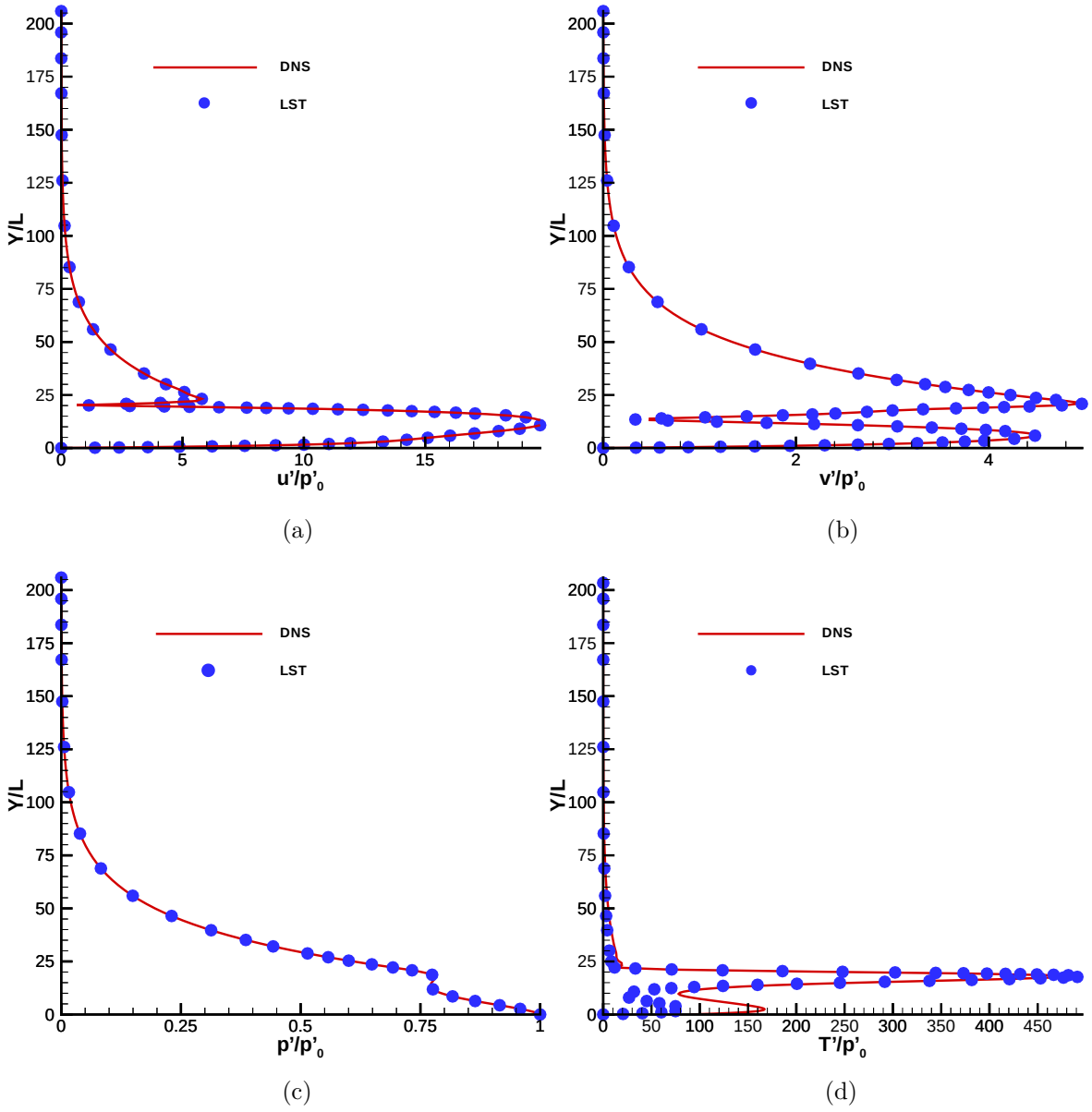

Figure 12: Comparisons of superimposed disturbance profiles for mode S with the eigenfunction of mode S obtained from LST: (a) streamwise velocity; (b) wall-normal velocity; (c) pressure; (d) temperature.

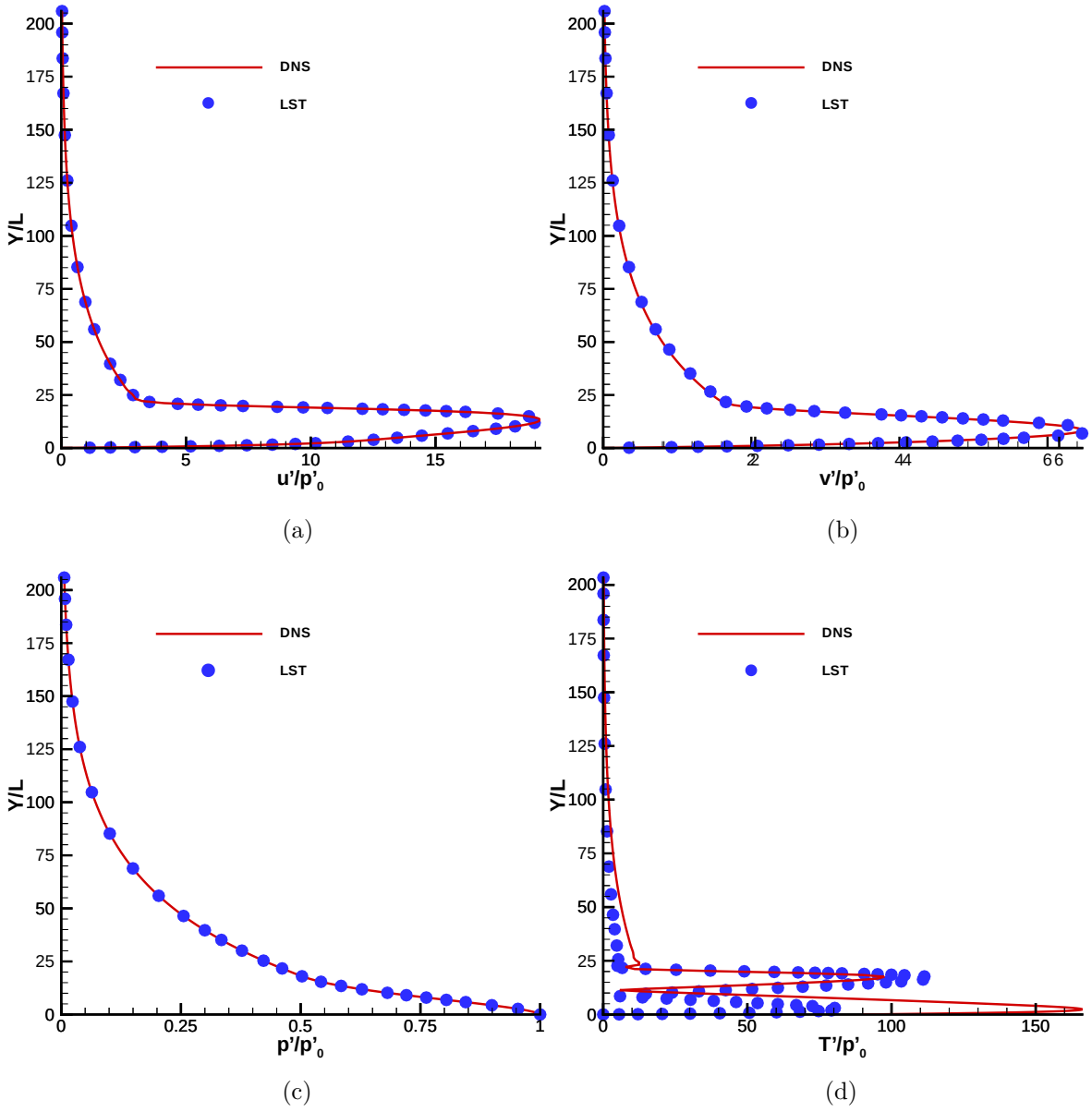

Figure 13: Comparisons of superimposed disturbance profiles for mode F with the eigenfunction of mode F obtained from LST: (a) streamwise velocity; (b) wall-normal velocity; (c) pressure; (d) temperature.

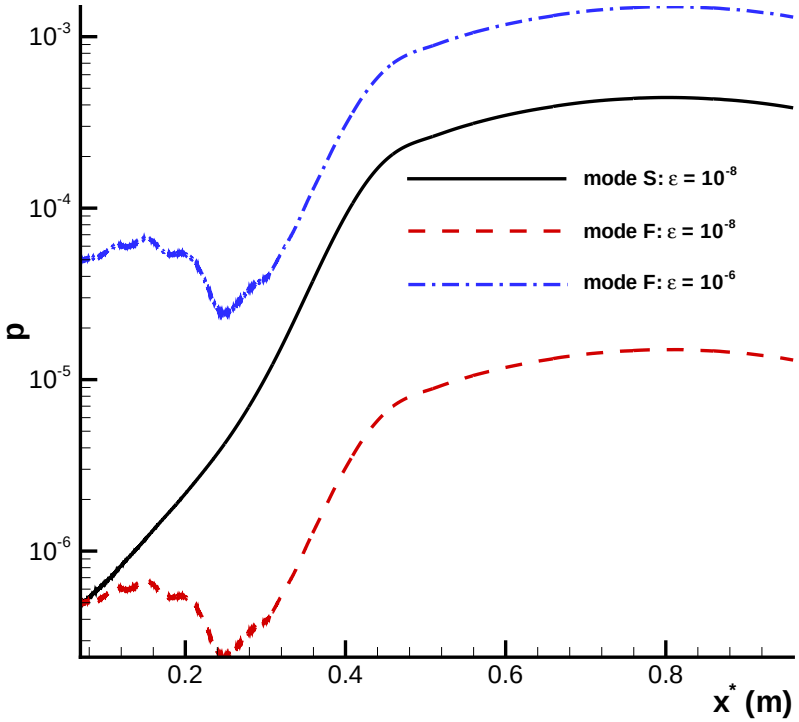

Figure 14: Spatial developments of superimposed mode S and mode F.

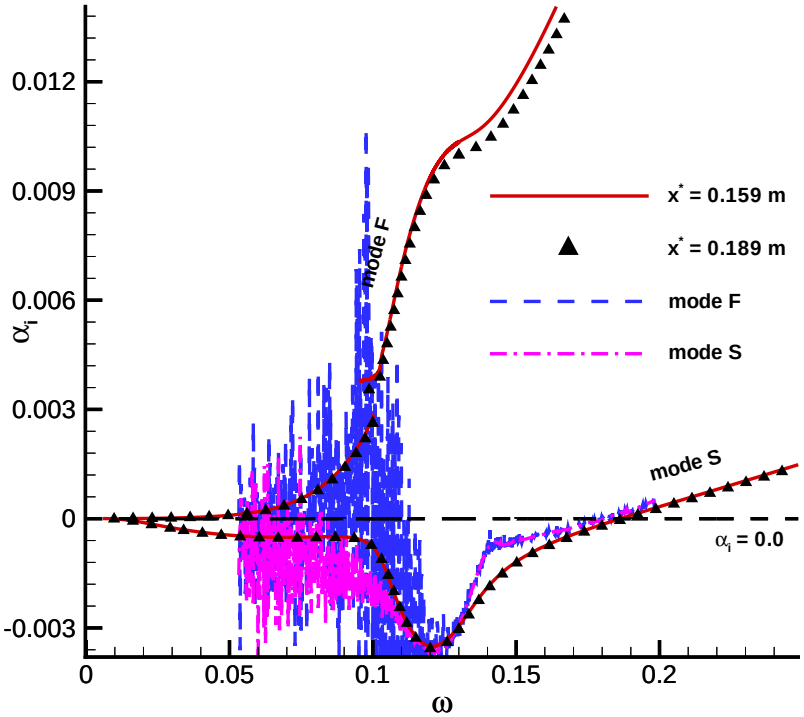

Figure 15: Comparison of the growth rate calculated from stability simulations with that obtained from LST for superimposed mode S and mode F.

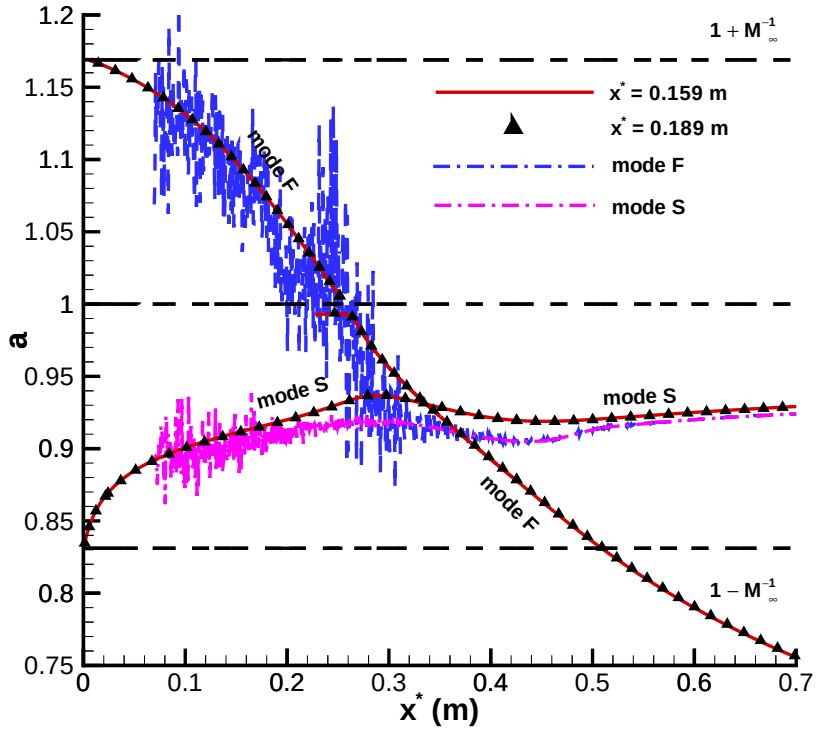

Figure 16: Comparison of the phase velocity calculated from stability simulations with that obtained from LST for superimposed mode S and mode F.

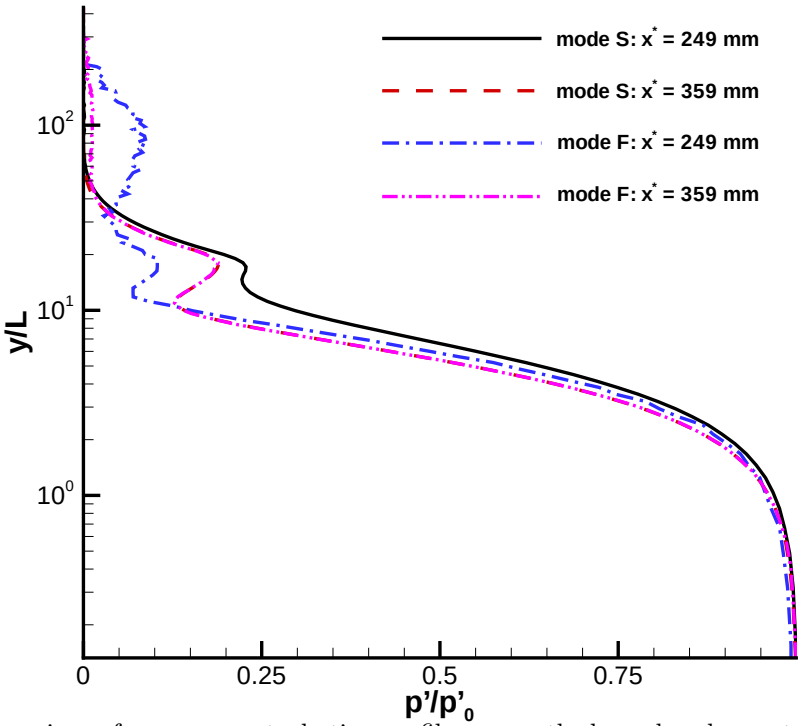

Figure 17: Comparison of pressure perturbation profiles across the boundary layer at two locations for superimposed mode S and mode F.

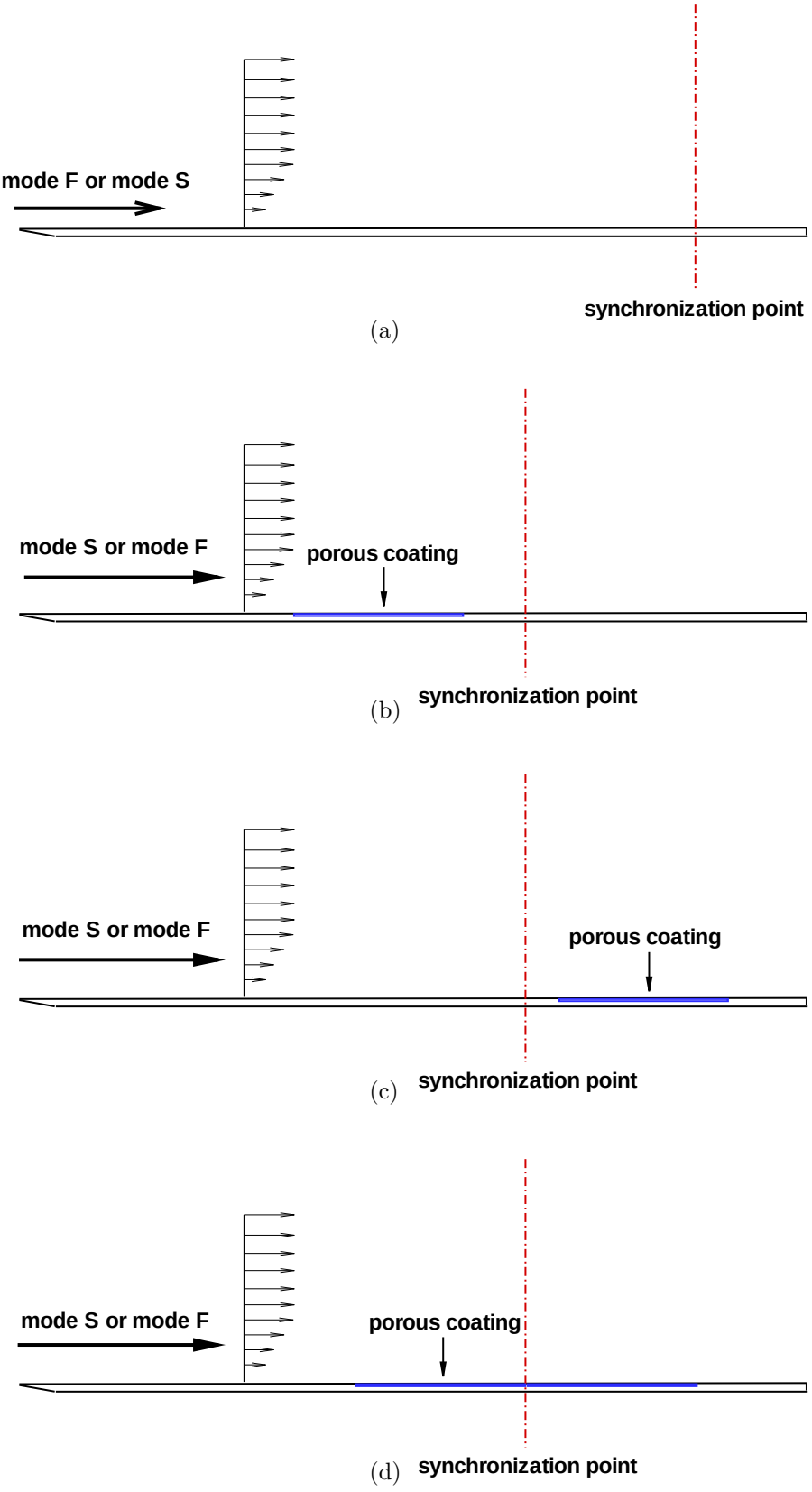

Figure 18: A schematic of porous coating locations and the synchronization point for the four types of stability simulations: (a) type 1; (b) type 2; (c) type 3; (d) type 4.

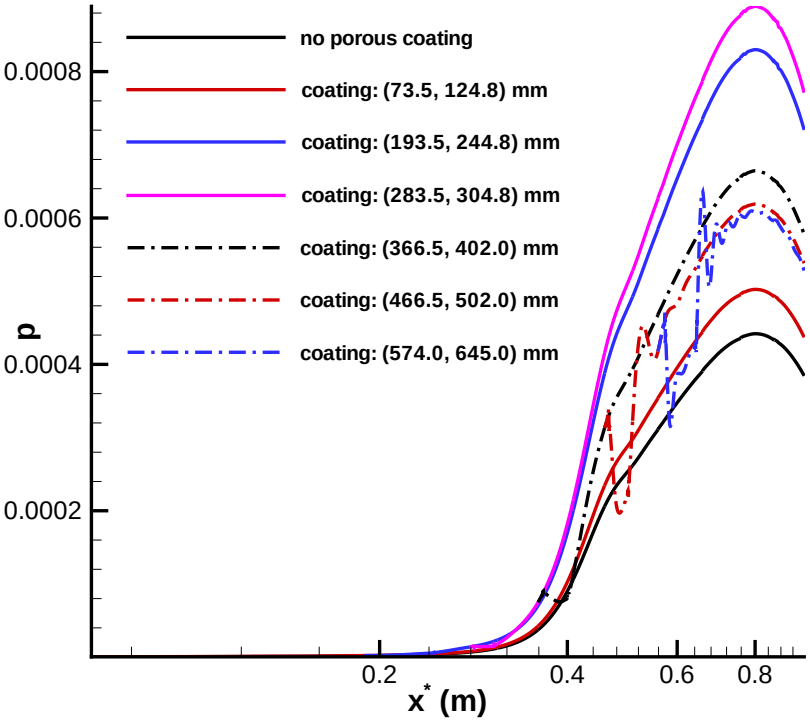

Figure 19: Amplitude distributions of pressure perturbation along the flat plate for the six cases of stability simulations.

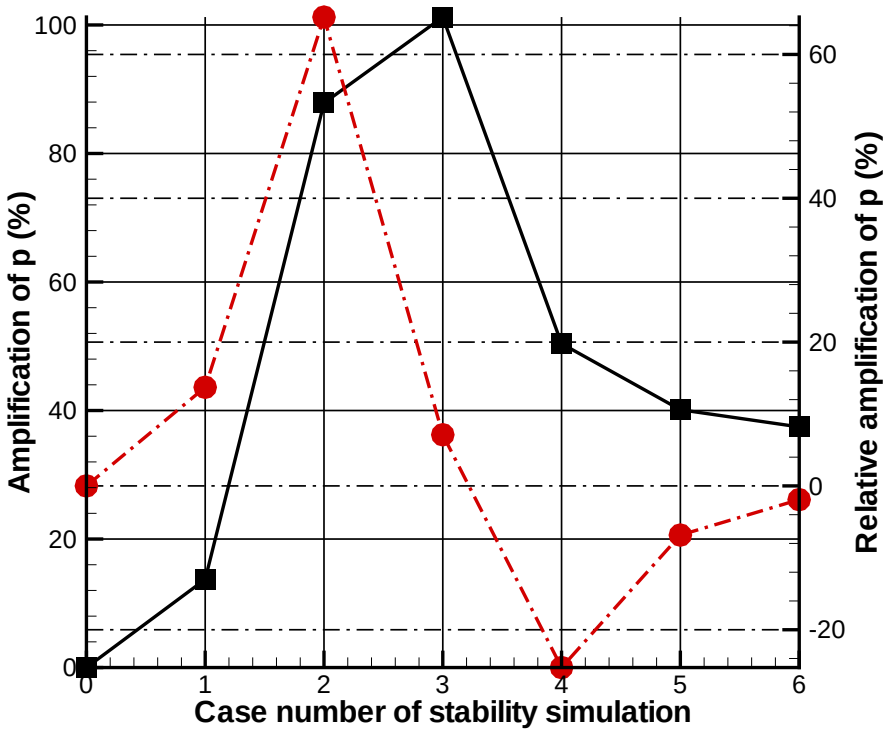

Figure 20: Amplification ratios of porous coating on the spatial development of mode S (amplification: rectangular, relative amplification: circular).

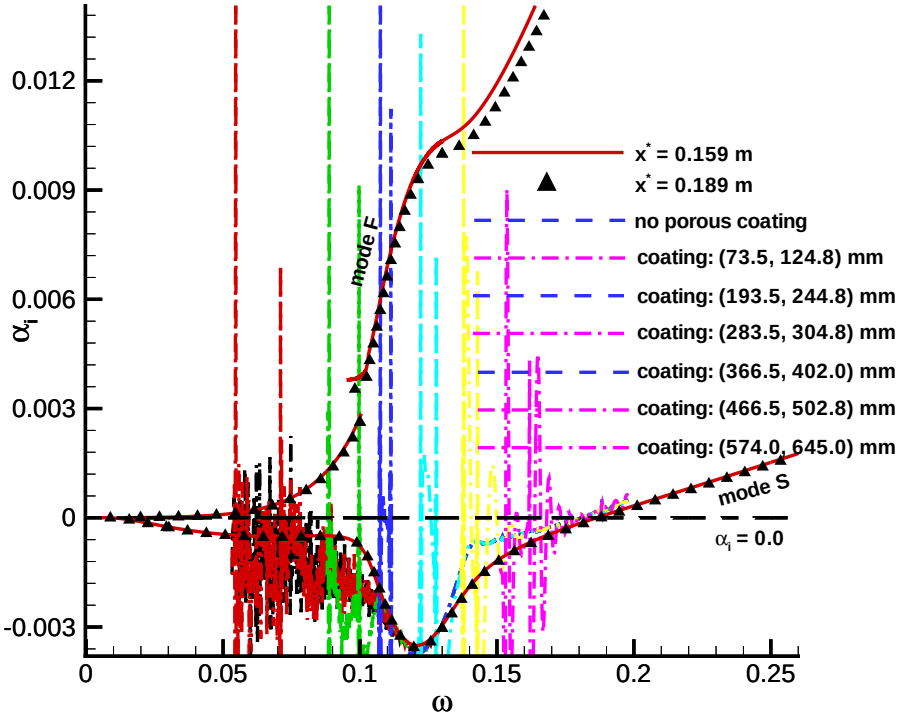

Figure 21: Comparison of the growth rate calculated from stability simulations with that obtained from LST for the six cases of stability simulations.

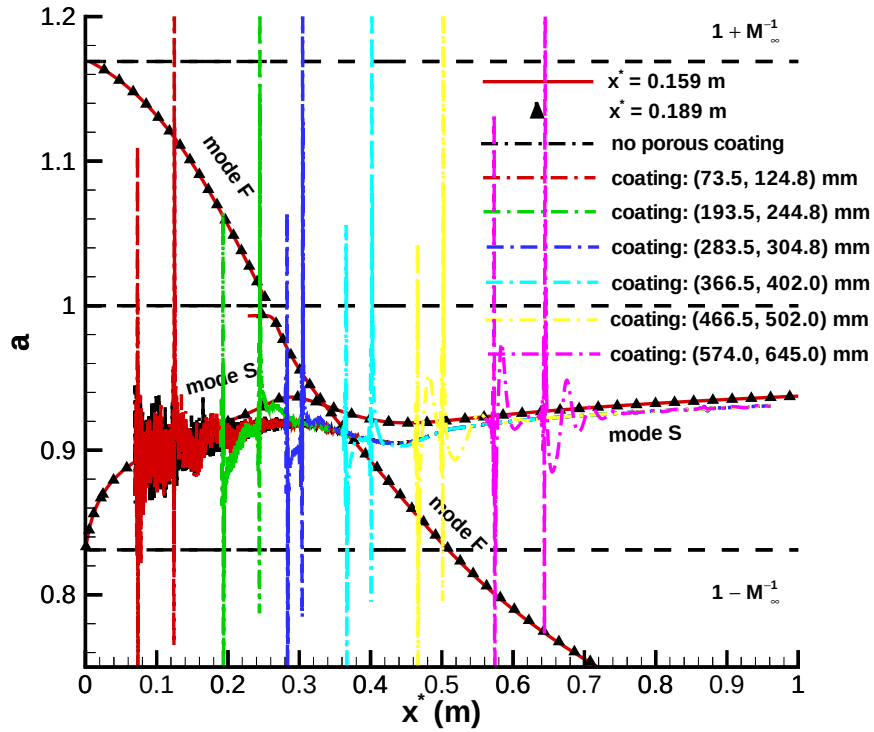

Figure 22: Comparison of the phase velocity calculated from stability simulations with that obtained from LST for the six cases of stability simulations.

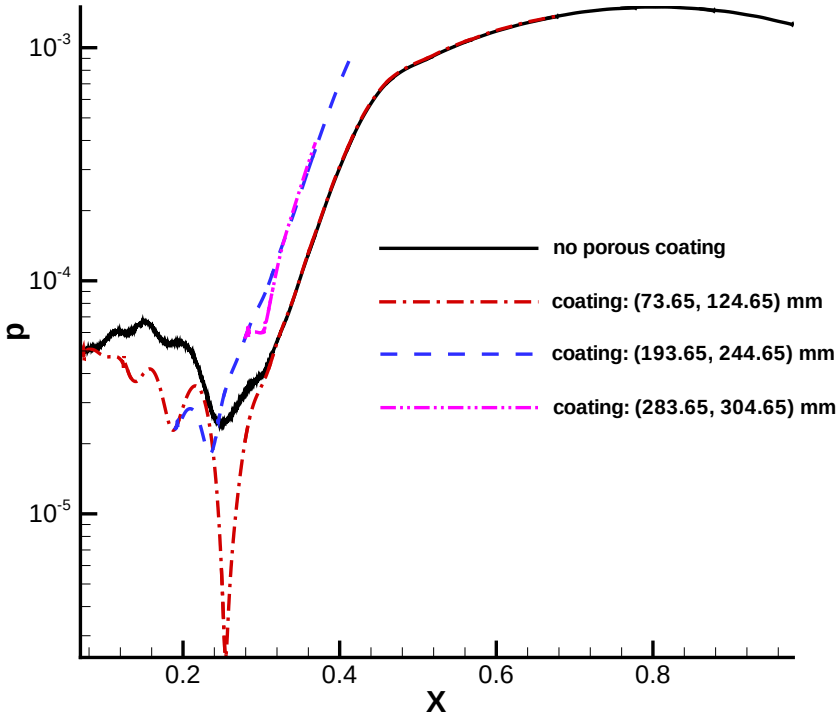

Figure 23: Amplitude distributions of pressure perturbation along the flat plate for the four cases of stability simulations.

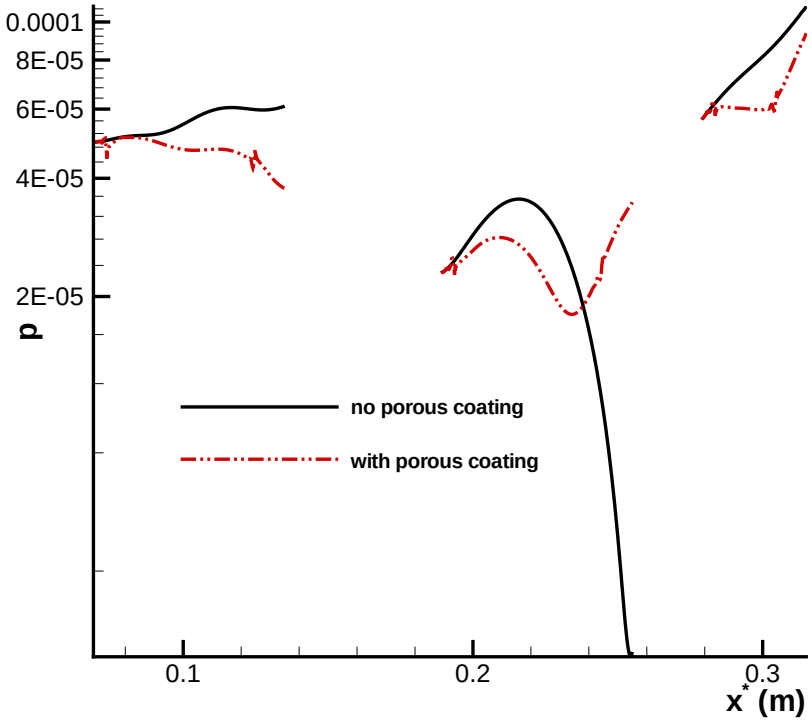

Figure 24: Comparison of pressure perturbation amplitude obtained from stability simulation with porous coating with that of mode F without porous coating.

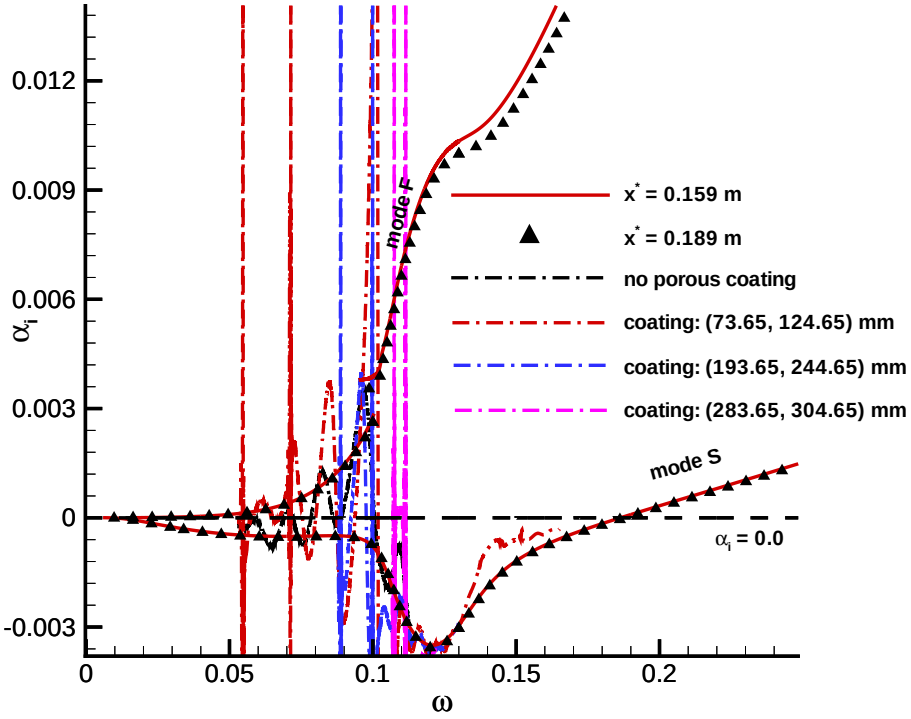

Figure 25: Comparison of the growth rate calculated from numerical simulation results with that obtained from LST for the three cases of stability simulations.

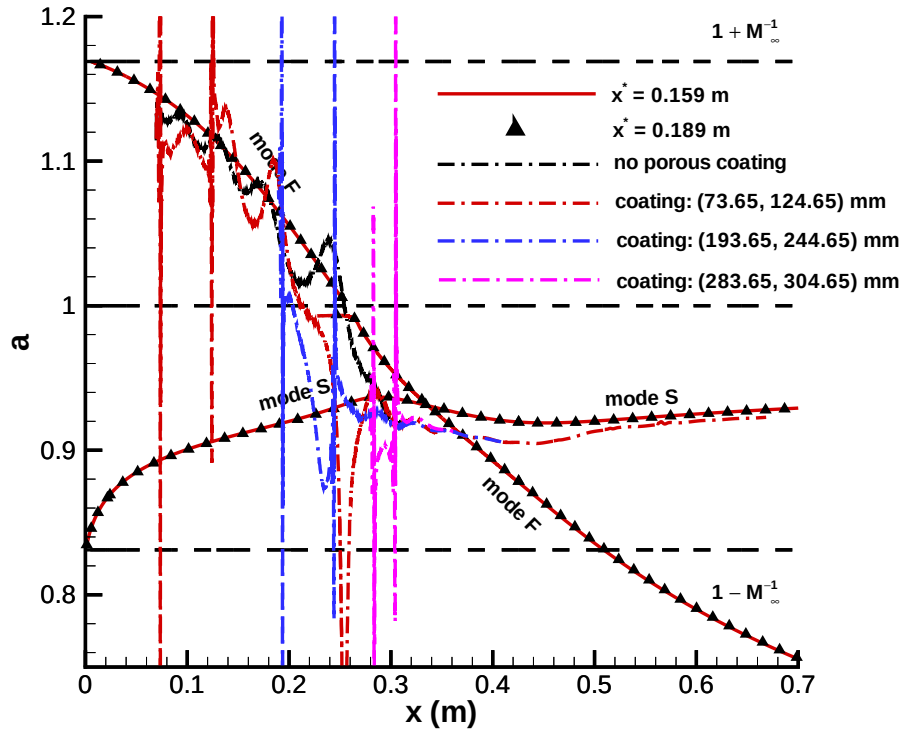

Figure 26: Comparison of the phase velocity calculated from numerical simulation results with that obtained from LST for the three cases of stability simulations.